RSC Advances

ROYAL SOCIETY OF CHEMISTRY

PAPER

View Article Online
View Journal | View Issue

Cite this: *RSC Adv.*, 2026, **16**, 1172

Computational optimization of $MASnI_3$ perovskite solar cells using SCAPS-1D simulations and machine learning techniques

Benjer Islam,[a] Tanvir Mahtab Khan, *[a] Md. Mountasir Rahaman[b] and Sheikh Rashel Al Ahmed *[a]

The lead-free methylammonium tin iodide ($MASnI_3$) has gained significant interest in perovskite solar cell (PSC) technology due to its ideal band gap and environmentally friendly composition, offering a promising alternative to traditional lead-based perovskites. In this computational work, the SCAPS-1D simulator is utilized to create and assess several PSC structures by merging two electron transport layers and three hole transport layers. Among them, the $MASnI_3$-based device architecture of Al/FTO/WS_2/$MASnI_3$/Zn_3P_2/Ni provides superior performance, including efficiency of 32.30%, fill factor (FF) of 87.35%, short-circuit current density (J_{sc}) of 34.19 $mAcm^{-2}$ and open-circuit voltage (V_{oc}) of 1.08 V. The influence of thickness, carrier density, defect concentration, and carrier lifetime of the $MASnI_3$ perovskite layer on the photovoltaic performance metrics is investigated meticulously. Furthermore, the effects of interface recombination, operating temperature, and capacitance–voltage (C–V) and capacitance–frequency (C–F) on the performance characteristics of the proposed structure are analyzed. Moreover, we present a comparative analysis conducted among three machine learning algorithms to identify the model that provides the highest accuracy in predicting the efficiency of the specified device. The results demonstrate that the XGBoost model achieves superior performance, yielding an R^2 value of 0.9999, along with a low mean squared error (MSE) of 0.0092 and mean absolute error (MAE) of 0.051. In addition, the individual influence of several input parameters on the device efficiency has been assessed using the feature importance method. Among the evaluated features, defect density emerged as the most influential parameter, indicating that it plays a significant role in defining the overall performance of the photovoltaic (PV) device.

Received 23rd September 2025
Accepted 19th December 2025

DOI: 10.1039/d5ra07200j

rsc.li/rsc-advances

1. Introduction

The worldwide transition to renewable energy has been accelerated by the urgent necessity to alleviate global warming and decrease reliance on fossil fuels.[1,2] Solar energy is one of the most abundant and sustainable renewable sources.[3] Scientists are diligently investigating different substances and device structures for effectively harvesting sunlight. Based on the materials and manufacturing processes, scientists have already evaluated various solar cell types.[4] Among them, the third-generation solar modules, particularly perovskite solar cells (PSCs), are garnering focus for their low production costs, experimental reproducibility, and high efficiency.[2,5] Perovskite materials, with the generic synthesis ABX_3, where 'A','B', and 'X' are respective cation, metal ion and halide, have revolutionized solar cell research.[1,6] The quick development of solar cells made of perovskites, with their efficiency soaring from 3.8% in 2009 to above 26% in just over a decade, reveals their exceptional optoelectronic properties and potential to compete with the traditional silicon-based photovoltaics.[7,8] Among the various perovskites, the methylammonium tin iodide ($MASnI_3$ or $CH_3NH_3SnI_3$) emerges as a lead-free perovskite alternative, addressing toxicity concerns associated with lead-based counterparts.[9] Additionally, $MASnI_3$ exhibits a suitable bandgap (~1.3 eV), high carrier mobility, and strong absorption in the visible spectrum, making it an ideal contender for efficient and eco-friendly PSCs.[9,10] Despite the $MASnI_3$-based PSCs demonstrating excellent PV properties, the Sn^{2+} ion of the $MASnI_3$ layer is oxidized into Sn^{4+} in an open environment.[11] This instability issue in tin-based perovskites can be effectively mitigated through optimized fabrication techniques, including the incorporation of tin fluoride (SnF_2) or tin iodide (SnI_2), which helps to suppress Sn^{2+} oxidation.[12,13]

Furthermore, the Goldschmidt tolerance (t) and octahedral factors (μ) are widely used to describe the stability of perovskite material.[14–16] For stable perovskite crystal structure, the value of

[a]*Department of Electrical, Electronic and Communication Engineering, Pabna University of Science and Technology, Pabna, 6600, Bangladesh. E-mail: tanvirshaikat92@gmail.com; rashel@pust.ac.bd*

[b]*Department of Computer Science & Engineering, University of Asia Pacific, 74/A Green Rd, Dhaka, 1205, Bangladesh*

t and μ should be in the range of $0.8 < t < 1.0$ and $0.414 < \mu < 0.732$.[15–17] Moreover, non-perovskite structure with intermolecular distortion forms when the tolerance factor is less than 0.8 and greater than 1.[14,16] However, the value of t and μ for $MASnI_3$ crystal structure is 0.904 and 0.555. Which falls between the ideal range of Goldschmidt tolerance and octahedral factors.[18] Additionally, among the Sn-based perovskite materials, $MASnCl_3$ and $MASnBr_3$ provides better stability compared to the $MASnI_3$, due to their higher tolerance factor close to 1.[18,19] However, $MASnI_3$ has often been regarded as the most promising of the $MASnX_3$ perovskites for solar-cell applications because of its favorable bandgap (~1.3 eV) and strong light absorption, which together support relatively high short-circuit current densities (J_{sc}) and good carrier transport properties.[20]

The initial $MASnI_3$-based PSC was fabricated by Noel *et al.* in 2014 and attained a PCE of 6.4% with a V_{oc} of 0.88 V.[21] In the same year, an additional research obtained an PCE of 5.23% for the $MASnI_3$-based PSC with Spiro-OMeTAD as an HTL.[22] The PCE of 5.44% is achieved for the structure of $TiO_2/MASnI_3$/Spiro-OMeTAD with V_{oc} of 0.716 V, J_{sc} of 15.18 mA cm^{-2}, and FF of 50.07%.[23] In 2019, the mesoporous $MASnI_3$-based PSCs were fabricated with excellent reproducibility, demonstrating a maximum efficiency of 7.13%.[24] In addition to the experimental studies, several research groups perform numerical investigation to improve the device performance significantly. By systematically optimizing several layer parameters, researchers have reported theoretical efficiencies exceeding 25%, which are significantly higher than current experimental values.[4,9,25–31] These findings not only highlight the strong potential of $MASnI_3$ as a viable lead-free absorber but also provide valuable guidelines for experimentalists aiming to close the gap between theoretical and practical efficiencies.

A significant problem that degrades the efficiency of heterojunction PSCs is carrier recombination at the rear contact. Therefore, improving their performance requires careful optimization of the structural design, material properties, and carrier transport mechanisms.[32,33] One effective approach is to use suitable transport layers to ensure proper alignment of band with the absorber layer. In this case, we can replace the commonly used toxic CdS electron transport layer (ETL) with environmentally friendly, non-toxic alternatives, which can provide appropriate band arrangement at the absorber/ETL interface.[34–36] Additionally, reducing the energy barrier at the interface of absorber/back contact helps suppress minority carrier recombination, thereby improving overall cell efficiency.[32,33,37] Adding an interlayer within the absorber and back contact can effectively lower the Schottky barrier and improve interface quality in heterojunction structures.[38] Moreover, the integration of heavily doped HTLs at the rear side of heterojunction PSCs has been shown to enhance carrier collection by minimizing surface recombination through better band alignment.[39–42]

In the past few years, machine learning (ML) has been recognized as a transformational method in the field of photovoltaic research, offering a data-driven alternative to accelerate the discovery and optimization of materials and device architectures.[43] By learning patterns from existing datasets, ML models can predict key performance parameters, identify critical material properties, and uncover complex nonlinear relationships that are difficult to capture through conventional methods.[31,44] In the context of PSCs, ML enables the rapid screening of material candidates, optimization of device layer properties, and performance prediction under various operating conditions. In recent years, numerous research groups have incorporated a variety of ML algorithms into PV technology to evaluate both the predictive accuracy of models and the influence of individual physical variables on the performance metrics of PSCs.[31,43–51] This approach not only minimizes the time and expenses related to experimental development but also provides deeper insights into the physical mechanisms governing device behavior.[43,47] Incorporating ML into the design workflow of perovskite solar cells provides a promising pathway for developing high-performance, resilient, and scalable photovoltaic technologies.

This study employs SCAPS-1D to architect and evaluate the performance of $Al/FTO/WS_2/MASnI_3/Zn_3P_2/Ni$ heterojunction PSC. Here, heavily doped p^+-type Zn_3P_2 is employed as a rear passivation layer to optimize the band alignment with the $MASnI_3$ active layer.[52,53] A minimal valence band offset (VBO) at the $Zn_3P_2/MASnI_3$ junction is observed, which facilitates efficient hole extraction from the absorber to the rear contact, ultimately contributing to enhanced device performance. Moreover, its key advantages include a suitable bandgap, high hole mobility, non-toxicity, low cost, and improved device stability.[36,51] Additionally, WS_2 is utilized as an alternative to the conventional CdS ETL in combination with the $MASnI_3$ absorber. It is a promising electron transport layer due to its non-toxic nature, cost-effectiveness, high electrical conductivity, suitable bandgap, and excellent carrier mobility.[53,54] However, the influences of perovskite layer thickness, defect density, doping concentration, and the device temperature and parasitic resistances on the suggested solar cell performance metrics are also explored in this numerical investigation. It also incorporates ML techniques, utilizing SCAPS-generated data to train and evaluate models and determine the most influential physical parameters, which are highly beneficial for the experimental scientist to design highly efficient PV cells without depending on time consuming trial and error processes.

2. Methodology for simulation

2.1. SCAPS-1D simulation

In order to develop and study the heterojunction PSC structure of $Al/FTO/WS_2/MASnI_3/Zn_3P_2/Ni$, we have used user-friendly and reliable SCAPS-1D simulation software.[55] The software can provide various electrical characteristics, such as external quantum efficiency (EQE), capacitance–voltage (C–V), capacitance–frequency (C–F), current density–voltage (I–V), and operating temperature. Moreover, The Poisson equation, drift diffusion, and the continuity equations governing electron and hole behavior form the foundation of this simulator.[35,56]

$$\frac{d^2}{dx^2}\Psi(x) = \frac{e}{\varepsilon_0\varepsilon_r}p(x) - n(x) + N_D - N_A + \rho_p - \rho_n \quad (1)$$

where ψ, ε_0, and ε are denoted as electrostatic potential, permittivity of vacuum, and semiconductor, respectively. N_D and N_A are respective donor and acceptor density.

$$\frac{\partial n}{\partial t} = -\frac{\partial}{\partial x}J_n - U_n + G,$$
$$\frac{\partial p}{\partial t} = -\frac{\partial}{\partial x}J_p - U_n + G \quad (2)$$

The letters U_n and G stand for recombination rate and carrier generation, respectively.

$$J_p = +\frac{\mu_p P}{q}\frac{\partial E_{Fp}}{\partial x},$$
$$J_n = -\frac{\mu_n n}{q}\frac{\partial E_{Fn}}{\partial x} \quad (3)$$

The current densities of the electron and hole are symbolized by J_n and J_p, respectively. μ_p and μ_n are the electron and hole mobility, respectively, and E_{Fp} and E_{Fn} are the Fermi levels of the hole and electron, respectively.[31,56]

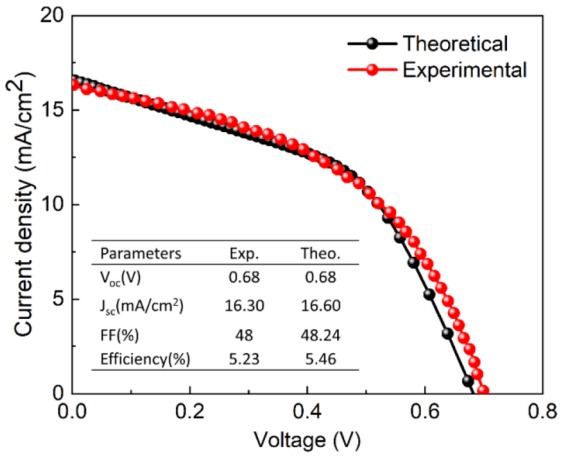

Fig. 1 Simulation and experimental J–V curves of $MASnI_3$-based PSCs.[31]

Firstly, SCAPS-1D is a widely accepted solar cell simulator, and the performance of solar cells designed using SCAPS-1D is compared with experimental results in numerous published works.[31,57–60] Their works found strong agreement between SCAPS-1D simulations and experimental results, which validated the reliability of our SCAPS-1D simulation in supporting and interpreting the experimental findings. Here, the comparison of J–V curves and performance metrics of experimental and simulation results is illustrated in Fig. 1.[31]

Our proposed Al/FTO/WS_2/$MASnI_3$/Zn_3P_2/Ni heterojunction cell structure is exhibited in Fig. 2(a). Additionally, in order to enhance PV performance, highly doped Zn_3P_2 plays the role of HTL that reduces the carrier recombination rate at the $MASnI_3$/Zn_3P_2 junction, WS_2 acts as an ETL, and FTO is used for the window layer. For front and back contact, we have selected Al and Ni with work function value of 4.06 eV and 5.35 eV, respectively.[61] However, precise temperature control is critical in thin-film deposition as it governs fundamental processes such as precursor decomposition, atomic surface mobility, and interfacial adhesion, directly determining the crystallinity, density, and electronic quality of each functional layer. In the fabrication of the proposed Al/FTO/WS_2/$MASnI_3$/Zn_3P_2/Ni solar cell, the temperature must be carefully tailored for each material. Commercially prepared FTO films, typically deposited *via* spray pyrolysis, achieve optimal polycrystalline conductivity when processed between 250 °C and 450 °C.[62] For the WS_2 electron-transport layer, sputtering or chemical vapor deposition at a substrate temperature near 200 °C yields films with greater crystal size, superior crystallinity, and reduced micro-strain, significantly enhancing their electronic properties.[63] Conversely, the tin-based perovskite $MASnI_3$ absorber presents a stringent thermal constraint; it can be deposited *via* hybrid evaporation at room temperature to form highly crystalline films without requiring SnF_2 additives or post-deposition annealing, thereby avoiding the thermal degradation of Sn^{2+}.[64] The Zn_3P_2 hole-transport layer, typically deposited by thermal evaporation, introduces another thermal consideration, as its decomposition and undesirable gas-phase reactions become significant above

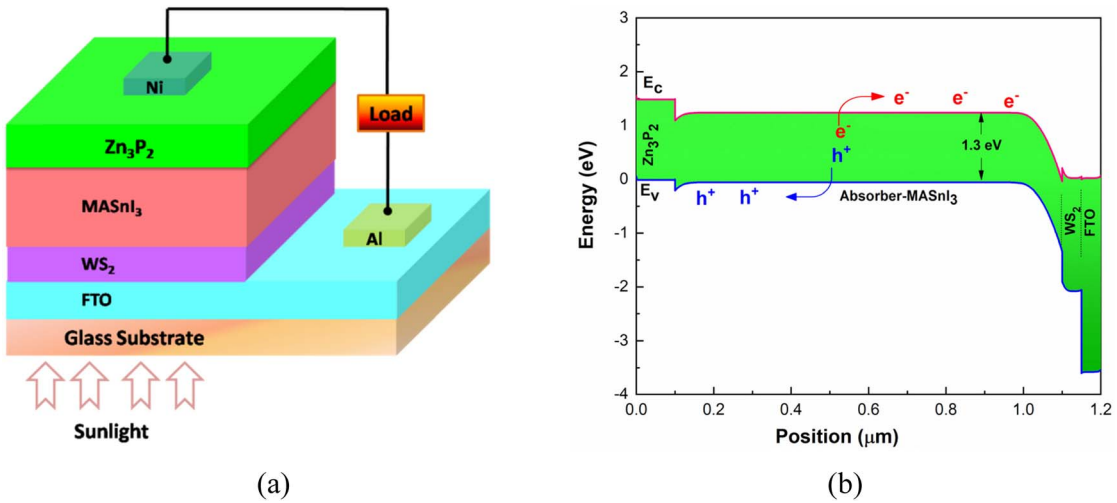

Fig. 2 (a) Structural schematic and (b) energy band diagram of proposed $MASnI_3$-based PSC.

Table 1 Physical parameters of different layers of the designed $MASnI_3$-based PSCs.[29,42,46,52,66–69]

		ETL			HTL		
Parameters (unit)	Window (FTO)	(CdS)	(WS_2)	Absorber ($MASnI_3$)	(Zn_3P_2)	(CuI)	(PEDOT:PSS)
Thickness (μm)	0.05	0.05	0.05	1	0.1	0.1	0.1
Band gap (eV)	3.6	2.4	2.1	1.3	1.5	3.1	2.2
Electron affinity (eV)	4	4.45	4.05	4.2	3.8	2.1	2.9
Dielectric permittivity (relative)	9	9	13.6	8.2	9	6.5	3.0
CB effective DOS (cm^{-3})	2.20×10^{18}	2.20×10^{18}	2.0×10^{18}	1.00×10^{18}	2.20×10^{18}	2.8×10^{19}	2.2×10^{15}
VB effective DOS (cm^{-3})	1.80×10^{19}	1.80×10^{19}	2.0×10^{18}	1.00×10^{18}	1.80×10^{19}	1.0×10^{19}	1.8×10^{18}
Electron thermal velocity ($cm\ s^{-1}$)	10^7	10^7	10^7	10^7	10^7	10^7	10^7
Hole thermal velocity ($cm\ s^{-1}$)	10^7	10^7	10^7	10^7	10^7	10^7	10^7
Electron mobility ($cm^2\ V^{-1}\ s^{-1}$)	100.00	100.00	100.00	1.6	1	100	0.02
Hole mobility ($cm^2\ V^{-1}\ s^{-1}$)	25.00	25.00	25	1.6	3.8	43.9	0.004
Donor density, N_D (cm^{-3})	10^{18}	10^{18}	10^{18}	0	0	0	0
Acceptor density, N_A (cm^{-3})	0	0	0	10^{17}	10^{19}	10^{18}	10^{18}
Defect type		Neutral	Neutral	Neutral	Neutral	Neutral	Neutral
Energetic distribution		Gaussian	Gaussian	Gaussian	Gaussian	Gaussian	Gaussian
Defect density, N_t (cm^{-3})		10^{15}	10^{15}	[a]10^{14}	10^{15}	10^{15}	10^{15}

[a] Variable.

approximately 390 °C.[65] Finally, the Ni and Al metal contacts are deposited *via* thermal evaporation at room temperature to preserve the integrity of all underlying temperature-sensitive layers. This careful, descending thermal profile—from a high-temperature FTO substrate to room-temperature metal contacts—is essential to sequentially build a functional, multi-layered device without degrading previously deposited films.

Finally, with the aim of securing the highly efficient solar cells, higher CBO and lower VBO at the interface of HTL/absorber play a crucial part. The minor VBO and large CBO ensure the hindrance of the passage of electrons and boost the transportation of holes from the absorber to back terminal by conducting the HTL.[51] From the schematic energy band diagram, the CBO and VBO can be calculated. Fig. 2(b) illustrates the architecture of band alignment of our proposed $MASnI_3$ heterojunction PSC. It is transparent that the conduction band is higher for Zn_3P_2 HTL than $MASnI_3$ absorber. For the purpose of conducting the simulation, all the parameters of Table 1 for different materials have been gathered from previous theoretical and experimental studies.[29,42,46,52,66–69] On the other hand, Table 2 presents the interface parameters for both ETL and HTL with $MASnI_3$ absorber material. Under the sunlight of AM 1.5G and a standardized temperature of 300 K, the cell device is illuminated at 100 mW cm^{-2} of incident power density. The absorption coefficient (α) for each layer of the proposed PSC is calculated by the equation below.[36]

$$\alpha = A_\alpha \sqrt{(h\nu - E_g)} \quad (4)$$

where photon energy and energy band are implied by h_ν and E_g, respectively, and the pre-factor A_α is set to 10^5 cm^{-1} $eV^{-1/2}$ for every material. α is the amount of light that may pass through a medium before being absorbed. It is determined on the wavelength of the light and the material.[70] A semiconductor material possessing high

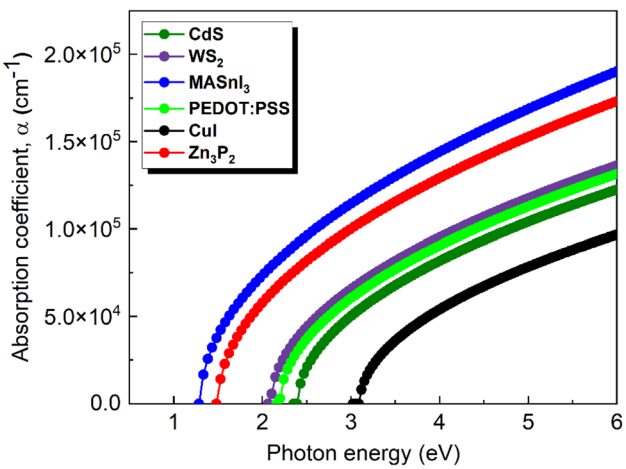

Fig. 3 Absorption coefficient of various layers of the proposed $MASnI_3$ solar cell as a function of photon energy.

Table 2 Parameters at the $WS_2/MASnI_3$ and $MASnI_3/Zn_3P_2$ interface

Parameters (unit)	$WS_2/MASnI_3$ junction	$MASnI_3/Zn_3P_2$ junction
Defect type	Neutral	Neutral
Capture cross-section of electrons (cm^2)	10^{-19}	10^{-19}
Capture cross-section of holes (cm^2)	10^{-19}	10^{-19}
Reference for defect energy level E_t	Above the highest E_v	Above the highest E_v
Energy with respect to reference (eV)	0.6	0.6
Total density (cm^{-2})	10^7 to 10^{17}	10^8 to 10^{18}

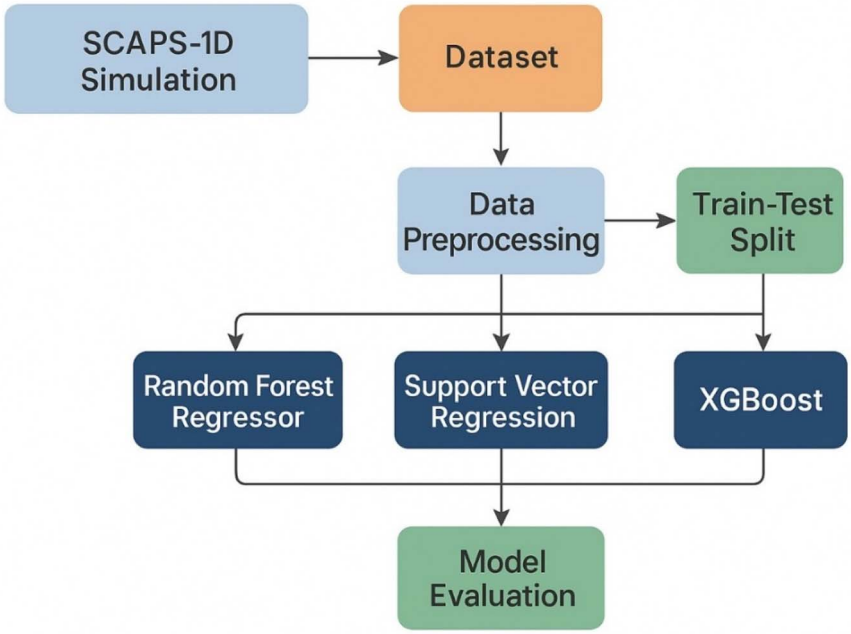

Fig. 4 Workflow of machine learning algorithms.

absorption coefficient characteristics absorbs comparatively more light than those materials that have low absorption coefficients. This process occurs when high-energy light photons drive electrons from the valence band to the conduction band, allowing them to travel more easily and improving light absorption. The value of α for the $MASnI_3$ film and different ETLs (CdS, WS_2) and HTLs (CuI, Zn_3P_2 and PEDOT:PSS) is collected from the SCAPS-1D simulator. Fig. 3 shows how the absorption coefficient varies with photon energy. Each layer ensures outstanding light gathering capabilities with a substantial absorption co-efficient (over 10^5 cm^{-1}). According to the figure, the $MASnI_3$ absorber has the greatest absorption coefficient among the various layers.

2.2. Machine learning algorithm

In this study, a structured machine learning workflow was developed to predict the power conversion efficiency (PCE) of the $MASnI_3$-based solar cell using the dataset generated from SCAPS-1D simulations. The workflow begins with the import of key Python libraries required for data processing, model development, and visualization. Pandas and NumPy were utilized for data handling, scikit-learn for preprocessing and classical regression models, XGBoost for gradient-boosted regression, matplotlib and seaborn for plotting. The dataset was initially loaded using pandas and examined for missing values. To ensure data consistency and avoid bias during model training, all rows containing missing entries were removed using the *dropna()* method. Following data cleaning, an 80 : 20 train–test split was performed using *train_test_split*, with a fixed random state to maintain reproducibility. Because machine learning models—particularly distance-based and gradient-based regressors—are sensitive to feature scaling, all input features were standardized using *StandardScaler*, transforming them to zero mean and unit variance to improve training stability and convergence.

Three regression algorithms were implemented to estimate device efficiency based on the selected physical parameters: Random Forest Regressor (RF), Support Vector Regression (SVR), and Extreme Gradient Boosting (XGBoost). Each model was trained on the training subset and subsequently evaluated on the unseen test subset to assess predictive generalization. Model performance was quantified using three widely accepted regression metrics: the coefficient of determination (R^2), mean squared error (MSE), and mean absolute error (MAE). Here, R^2 measures the goodness of fit, and MSE and MAE quantify the magnitude of prediction errors.[71] Together, these metrics provide a comprehensive assessment of each model's predictive capability. Here, Fig. 4 presents the overall workflow of the study, illustrating each step of the process—from data generation to model development and performance evaluation.

3. Result and evaluation

3.1. Performance improvement of $MASnI_3$ perovskite solar cell

The performance of a solar module is fundamentally influenced by how quickly charge carriers recombine. Reducing the intensity of recombination enhances performance. Recombination is affected by the factors such as band alignment and barrier height at the p–n junction. Selecting suitable HTL and ETL is crucial in mitigating carrier recombination. This reduction in the rate of recombination is reflected in the improved current–voltage (*J–V*) properties and external quantum efficiency (EQE) metrics.

Fig. 5(a) illustrates the *J–V* characteristics of $MASnI_3$-based heterojunction perovskite solar cells incorporating numerous ETLs such as WS_2 and CdS, and HTLs including PEDOT:PSS, Zn_3P_2 and CuI. The PV outputs of cells with HTLs are notably

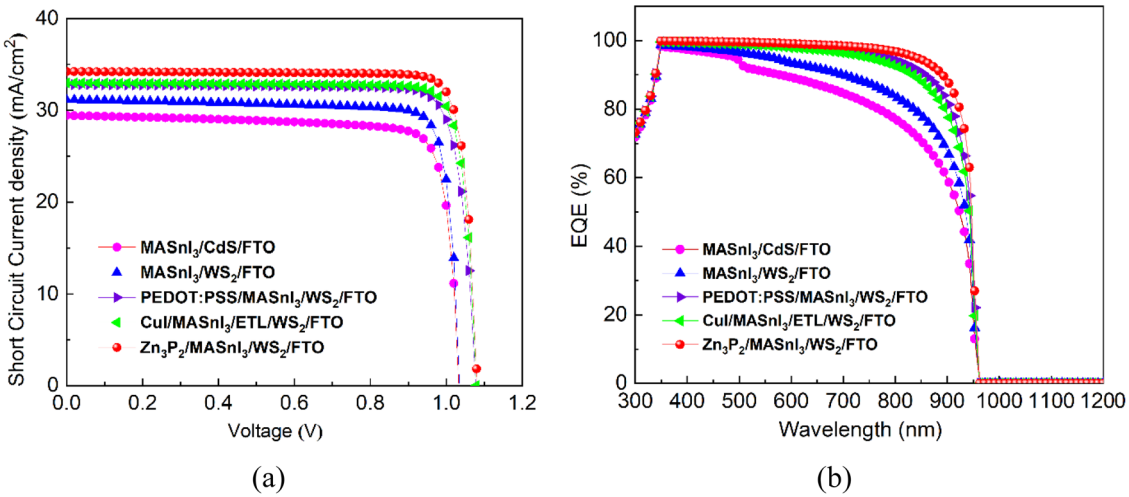

Fig. 5 Comparative analysis of (a) J–V characteristics and (b) EQE responses of $MASnI_3$-based PSCs incorporating different ETLs and HTLs.

Table 3 PV performance parameters and CBO and VBO values of $MASnI_3$-based architecture with various ETLs and HTLs

Architectures	CBO (eV)	VBO (eV)	V_{oc} (V)	J_{sc} (mA cm^{-2})	FF (%)	PCE (%)
Al/FTO/CdS/$MASnI_3$/Ni	−0.25	—	1.0342	29.44	83.14	25.32
Al/FTO/WS_2/$MASnI_3$/Ni	0.15	—	1.0361	31.16	85.38	27.57
Al/FTO/WS_2/$MASnI_3$/PEDOT:PSS/Ni	1.3	0.4	1.0785	32.81	85.38	30.21
Al/FTO/WS_2/$MASnI_3$/CuI/Ni	2.1	0.3	1.08	32.97	86.80	30.91
Al/FTO/WS_2/$MASnI_3$/Zn_3P_2/Ni	0.4	0.2	1.0815	34.19	87.35	32.30

superior to those of the conventional cell structure without an HTL, as clearly depicted in the figure. Performance metrics for each architecture are detailed in Table 3. The data also reveal that the J_{sc} for the $MASnI_3$/WS_2 cell configuration surpasses that of the configuration with a CdS ETL. Specifically, for WS_2 ETL, a J_{sc} of 31.16 mAcm^{-2} and a V_{oc} of 1.0363 V are achieved, while the $MASnI_3$ solar cell with CdS ETL shows a J_{sc} of 29.44 mAcm^{-2} and a V_{oc} of 1.0342 V, respectively. Among all the configurations studied, the best performance is observed in the Ni/Zn_3P_2/$MASnI_3$/WS_2/FTO/Al architecture, which records efficiency of 32.30%, an FF of 87.35%, a J_{sc} of 34.19 mAcm^{-2} and a V_{oc} of 1.08 V. The decrease in carrier recombination losses within the heterojunction is responsible for these higher efficiencies in cells containing HTLs. Minority electron passage toward the rear contact is blocked by a significant potential barrier created by a highly doped HTL placed at the rear of the absorber.[39]

The role of ETLs and HTLs on the output characteristics of $MASnI_3$ cells is highlighted through their EQE variation with wavelength, as illustrated in Fig. 5(b). The EQE reflects the capability of PV devices to produce and collect charge carriers from photons of specific energies.[72] The EQE profiles are shown across the 300–1200 nm wavelength range. The functionality of $MASnI_3$-based solar cells has been evaluated using CdS and WS_2 as ETLs. The results indicate that the $MASnI_3$/WS_2 solar cell outperforms the $MASnI_3$/CdS cell. This improvement is attributed not to higher optical transparency, but to the favorable band alignment and reduced interfacial recombination provided by WS_2 compared to CdS. With a band gap of ~2.1 eV, WS_2 still absorbs part of the visible spectrum, but its superior electronic properties and efficient charge transfer to $MASnI_3$ enhance the overall device efficiency. Additionally, the EQE curve for the Zn_3P_2 HTL combined with the $MASnI_3$ absorber demonstrates a greater performance enhancement in the 700–900 nm wavelength range compared to other HTLs like CuI and PEDOT:PSS. This improvement attributes to the back surface field formed at the Zn_3P_2/$MASnI_3$ interface, which effectively collects more charge carriers from the absorber, leading to improved device performance. Moreover, when the incident photon energy is lower than the band gap of the absorber layer, the photons cannot be absorbed, leading the quantum efficiency (QE) to drop to zero. This effect is also observed in this study when the wavelength exceeds 950 nm.

The energy level diagram of the $MASnI_3$ perovskite, ETLs (CdS and WS_2), and HTLs (CuI, PEDOT:PSS, and Zn_3P_2) is shown in Fig. 6(a). Two types of band offsets, CBO and VBO, emerge at the interface and can be computed as follows.[73]

$$\Delta E_c = \Delta\chi \quad (5)$$

$$\Delta E_v = \Delta E_g - \Delta E_c \quad (6)$$

The parameter ΔE_g represents the band gap difference between the two interface materials, whereas $\Delta\chi$ corresponds to the difference in their electron affinities.

To ensure efficient electron transfer from the absorber to the front electrode, the CBO at the ETL/absorber interface must be minimal.[31,39,74] Specifically, a "cliff-like" band formation occurs at the ETL/perovskite interface when the CBO is negative, while

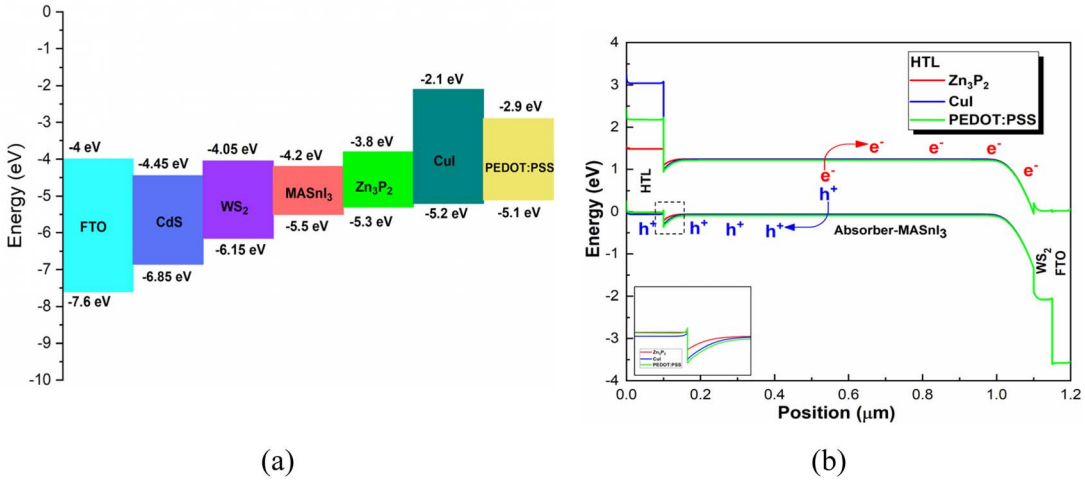

Fig. 6 (a) Energy-level arrangement in $MASnI_3$-based PSCs and (b) schematic representation of the band diagram for devices with HTLs.

an energy "spike-like" forms at the ETL/perovskite interface when the CBO is positive.[75–77] This "cliff" structure introduces interface recombination, which results in reduced PV performance.[78] By contrast, "spike" band alignment promotes efficient electron transfer from the perovskite layer to the front contact through the ETL; meanwhile it also reduces the amount of recombination at the ETL/perovskite interface.[76] In this study, the CBO at the $MASnI_3/WS_2$ interface is found to be 0.15 eV compared to −0.25 eV at the $MASnI_3$/CdS interface. As a result, the $MASnI_3$/CdS interface tends to form a "cliff-like" band alignment, while the $MASnI_3/WS_2$ interface exhibits a "spike-like" band configuration. This spike shape is favorable since it drops carrier recombination at the front junction, therefore boosting the overall efficiency of PSCs.[76,79] This evidence indicates that WS_2 is a more suitable candidate as an ETL, as it supports smooth electron transport. Furthermore, for effective hole transport from the absorber to the rear contact through the HTL, the CBO at the HTL/$MASnI_3$ interface needs to be positive, while the VBO should ideally be near zero or marginally negative.[31,39,74] The CBO and VBO values for all the interfaces are provided in Table 3. The CBO values for CuI, PEDOT:PSS, and Zn_3P_2 have been determined to be 2.1 eV, 1.3 eV, and 0.4 eV, respectively, while the respected VBO values are 0.3 eV, 0.4 eV, and 0.21 eV, respectively. It is clear that the value of VBO at the CuI/$MASnI_3$ and PEDOT:PSS/$MASnI_3$ interfaces is higher than the VBO at the $Zn_3P_2/MASnI_3$ interface. The small value of VBO at the $Zn_3P_2/MASnI_3$ interface may facilitate hole transport, thereby improving the overall PV performance of the solar cell. As a result, integrating a Zn_3P_2 HTL at the rear and a WS_2 ETL at the front of the absorber is recommended to significantly enhance the efficiency of $MASnI_3$-based PSCs. The schematic band diagram of $MASnI_3$-based PSCs with various HTLs is illustrated in Fig. 6(b). It is evident from the diagram that the VBO at the $Zn_3P_2/MASnI_3$ interface is smaller compared to other interfaces. Minimizing the VBO at the junction promotes seamless hole transport, thereby reducing interfacial resistance and enhancing overall device performance.[72,80]

Furthermore, to show that the proposed $MASnI_3$-based perovskite solar cell using WS_2 as the ETL and Zn_3P_2 as the HTL performs better than the other investigated material combinations, we used Nyquist plots to evaluate the effects of the conduction band offset (CBO) and valence band offset (VBO) at

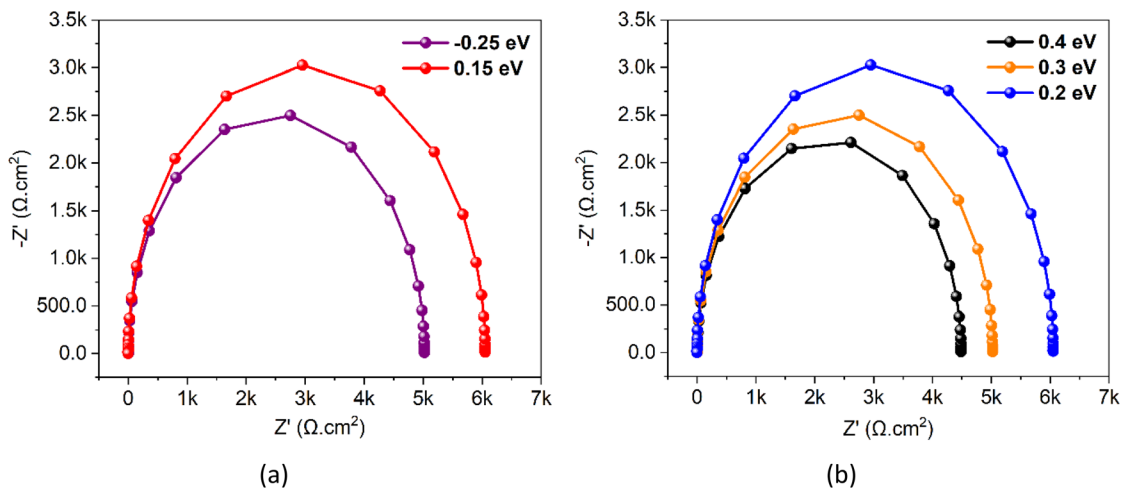

Fig. 7 Nyquist plots for different (a) CBO at the interface of $MASnI_3$/ETL and (b) VBO at the interface of HTL/$MASnI_3$.

the ETL/absorber and HTL/absorber interfaces, respectively. The Nyquist plots exhibit a typical semicircular pattern, where the left side corresponds to the high-frequency region and the right side represents the low-frequency region.[81] The simulation covers a frequency range from 1 Hz to 1 MHz, allowing us to interpret both charge-transport and recombination mechanisms accurately. The effects of CBO and VBO on the device impedance appear in Fig. 7(a) and (b). In these figures, the horizontal axis represents the real impedance (Z'), whereas the vertical axis denotes the imaginary impedance ($-Z'$).[82,83] Based on interface band-alignment considerations, a positive CBO at the ETL/absorber interface is essential because it creates a small spike that facilitates electron transport toward the front contact while reducing interface recombination.[83] Consequently, as shown in Fig. 7(a), the semicircle corresponding to a CBO of +0.15 eV at the $WS_2/MASnI_3$ interface appears larger than that formed from a CBO of −0.25 eV at the $CdS/MASnI_3$ interface, indicating lower recombination and improved electron extraction for WS_2.

Similarly, to minimize recombination at the back interface and ensure smooth hole extraction, the VBO at the HTL/absorber interface must be small and preferably close to zero.[31,39,74] As illustrated in Fig. 7(b), the semicircle associated with Zn_3P_2, which has a VBO of +0.2 eV, is larger than those corresponding to CuI (0.3 eV) and PEDOT:PSS (0.4 eV). This observation suggests that Zn_3P_2 offers reduced recombination and enhanced hole-transport capability compared with the other HTLs. Overall, based on the Nyquist-plot analysis, WS_2 as the ETL and Zn_3P_2 as the HTL demonstrate superior interface alignment and transport characteristics. As a result, the optimized device structure, $Al/FTO/WS_2/MASnI_3/Zn_3P_2/Ni$, achieves excellent photovoltaic performance, delivering a J_{sc} of 34.19 mA cm^{-2}, a V_{oc} of 1.08 V, a fill factor of 87.35%, and a power conversion efficiency of 32.30%.

Moreover, investigating the lattice mismatch between the absorber and other films is crucial for optimizing device performance. We have calculated the percentage of lattice mismatch using based on the equation bellow.[74,76]

$$\delta = \frac{2|\ a_s - a_e|}{a_s + a_e} \times 100\% \quad (7)$$

here, α_s refers to substrates' lattice constant on which the overlaid layer is deposited, and α_e signifies the lattice constant of the layer itself. Table 4 displayed mismatches of $MASnI_3$ absorber with HTLs (Zn_3P_2, CuI, and PEDOT:PSS) and ETLs (CdS and WS_2) and the least mismatch of $MASnI_3$ happens to be with Zn_3P_2 HTL and WS_2 ETL.[84–89] Therefore, the proposed $Ni/Zn_3P_2/MASnI_3/WS_2/FTO/Al$ cell structure exhibits a J_{sc} of 34.19 mA cm^{-2}, V_{oc} of 1.08 V, PCE of 32.30%, and FF of 87.35%.

Table 4 Lattice mismatch of $MASnI_3$ absorber with ETLs and HTLs.[84–89]

	Lattice parameters			
Layers	a (Å)	b (Å)	c (Å)	Lattice mismatch (%)
$MASnI_3$ (absorber)	8.73	8.95	12.5	—
WS_2 (ETL)	3.153	3.153	12.323	1.42%
CdS (ETL)	—	—	6.677	11.17%
Zn_3P_2 (HTL)	8.0785	8.0785	11.3966	7.75%
PEDOT:PSS (HTL)	4.28	11.41	3.96	9.12%
CuI (HTL)	6.14	6.14	6.14	34.83%

3.2. Optimization of absorber thickness and acceptor density (N_A) for enhancing $MASnI_3$-based perovskite solar cell performance

The impact of $MASnI_3$ absorber thickness on the performance of PV solar cells is systematically examined by shifting the thickness from 0.01 μm to 2 μm and is illustrated in Fig. 8(a). The study reveals that as the absorber thickness increases, all performance metrics improve, with the PCE rising from 10.71% to 32.76%, the FF enhancing from 85.01% to 87.16%, and the J_{sc} increasing from 10.32 mA cm^{-2} to 34.23 mA cm^{-2}. Conversely, the V_{oc} started to decline from 1.18 V to 1.06 V. The observed improvement in PCE, FF, and J_{sc} with increased thickness is ascribed to improved light absorption and more efficient charge carrier collection within the thicker absorber layer.[66,90,91] This trend continues up to a thickness of approximately 1.0 μm, beyond which the performance metrics stabilize, indicating a saturation point. In a thin absorber layer, the capacity for light absorption diminishes, resulting in a decrease in both J_{sc} and overall efficiency. The downturn in V_{oc} with growing thickness is likely results from intensified non-radiative carrier losses in the thicker absorber layer, which adversely affects the open-circuit voltage despite the gains in other performance parameters. Conversely, the increase in dark saturation current with greater thickness contributes to a decline in V_{oc}, contributing to greater electron–hole recombination.[39,92] The behavior of V_{oc} with varying absorber thickness can be explained using the equation bellow.[36]

$$V_{oc} = \frac{AK_BT}{q}\left[\ln\left(1 + \frac{J_{sc}}{J_0}\right)\right] \quad (8)$$

where the ideality factor is A, the fundamental charge is q, K_BT/q represents the thermal voltage, and J_0 indicates the reverse saturation current concentration.

This numerical study rigorously examines how the N_A Effects on PV solar cell performance metrics. The absorber doping is systematically changed over a range from 10^{12} to 10^{19} cm^{-3}, as illustrated in Fig. 8(b). The PCE remains constant at 28.92% as increasing of doping density from 10^{12} to 10^{15} cm^{-3}.

However, as the N_A further raises from 10^{15} to 10^{19} cm^{-3}, a significant rise in PCE is observed, escalating from 28.92% to 35.37%. This increase implies that a perfect range exists for carrier concentration, maximizing efficiency by boosting carrier generation and minimizing recombination losses.[74,91] Similarly, the FF and V_{oc} remain stable as the carrier concentration increases up to 10^{15} cm^{-3}. Beyond these thresholds, the FF increases from 84.36% to 88.97%, V_{oc} improves from 1.02 to 1.19 V, as the N_A rises from 10^{15} to 10^{19} cm^{-3}. The enhancement in FF results from a decrease in the series resistance of the solar cell, facilitating higher current flow with minimal resistive losses. The increase in V_{oc} results from a higher quasi-Fermi level splitting, enabled by diminished radiative recombination

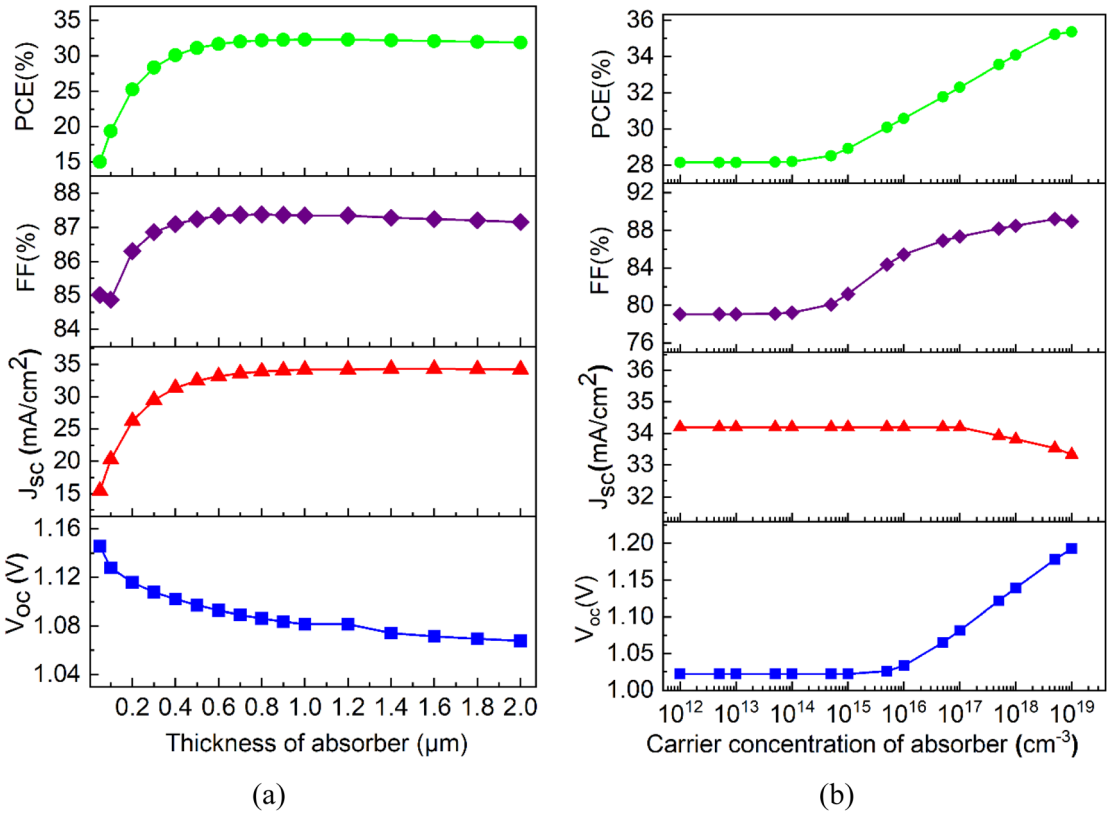

Fig. 8 Impact of absorber (a) thickness and (b) carrier concentration on $MASnI_3$-based PSC.

within the device.[76] The J_{sc} maintains a steady value up to a N_A of 10^{15} cm^{-3}, beyond which it experiences a slight decrease to 33.32 mA cm^{-2}. As doping density increases, more holes are created, leading to additional trap sites in the absorber layer, which could be the reason for the decline in J_{sc} at higher carrier concentrations.[66,72,93] Based on this analysis, the thickness and acceptor density of the absorber layer are chosen to be 1 μm and 10^{17} cm^{-3} respectively, for further exploration of the $MASnI_3$-based PSC.

3.3. The role of defect state (N_t) of absorber on $MASnI_3$-based PSC

Understanding the effect of defect density (N_t) in the $MASnI_3$ perovskite layer is vital for evaluating PV device performance. Introducing a considerable number of defects into the absorber significantly enhances the recombination rate within the solar cell leading to a significant drop in performance. Consequently, the increase in defect states impedes efficient charge extraction at the absorber/ETL interface, leading to a significant reduction in the solar cell's output characteristics.[39,74] Keeping all other factors constant, the value of N_t is changed from 10^{12} to 10^{18} cm^{-3} to investigate the impact on output metrics. Fig. 9 depicts the corresponding variation. It is evident from the figure that after reaching a defect level of 10^{14} cm^{-3}, all performance parameters begin to degrade significantly, whereas before this point, the degradation is more gradual. As the N_t rises from 10^{14} to 10^{18} cm^{-3}, the PCE and FF experience a sharp decline, dropping from 32.32% to 7.72% and from 87.35% to 67.42%, respectively. Meanwhile, at a defect density of 10^{12} cm^{-3}, the V_{oc} is 1.2 V and the J_{sc} is 34.88 mA cm^{-2}. When the N_t reaches to 10^{18} cm^{-3}, these values fall to 0.73 V for V_{oc} and 16.72 mA cm^{-2} for J_{sc}. Therefore, the value of N_t of the $MASnI_3$ absorber is selected to be 10^{14} cm^{-3}. At this concentration, the PCE is determined to be 32.30%, FF is 87.35%, the J_{sc} is 34.20 mA cm^{-2}, and the V_{oc} is 1.08 V.

3.4. Impact of thickness and defect density on carrier lifetime and diffusion length

In this numerical study, we explored the characteristics of carrier lifetime, and diffusion length in terms of the thickness and impurity state of the $MASnI_3$ absorber. The average period a minority carrier in a semiconductor material takes to recombine with an opposite charge carrier is define as carrier lifetime. Conversely, the diffusion length of a carrier in a material refers to the average distance an excited carrier travels before recombination occurs. Eqn (9) can be used to express and calculate the carrier lifetime.[70]

$$\tau_{n,p} = \frac{1}{\sigma_{n,p} N_t V_{th}} \quad (9)$$

where V_{th}, $\sigma_{n,p}$, and $\tau_{n,p}$ serves as thermal velocity of carriers, capture cross-section, and carrier lifetime and N_t denotes the absorber's defect state.

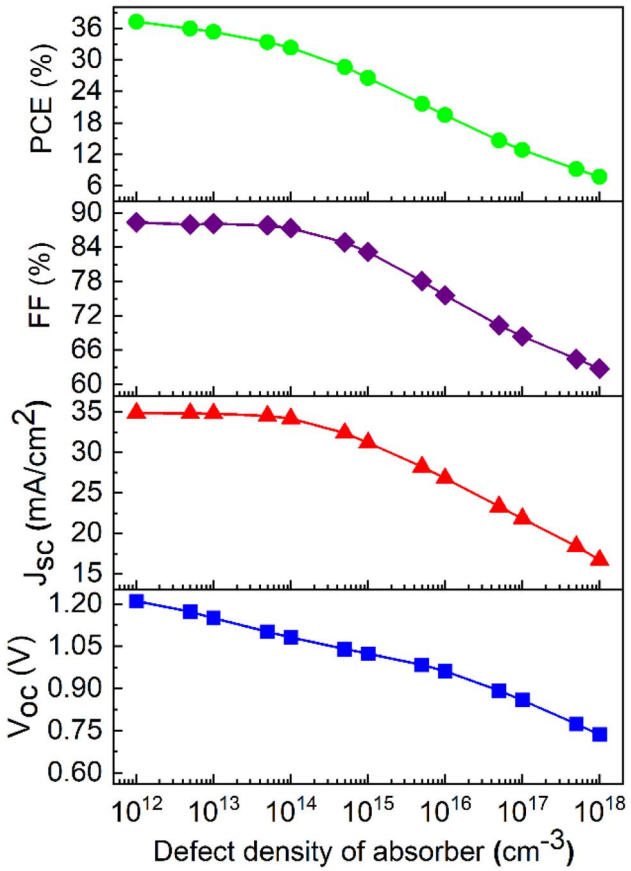

Fig. 9 Impact of absorber defect concentration on the performance of the $MASnI_3$-based PSC.

Diffusion length is a function of carrier lifetime and mobility, as shown in the following relation.

$$L_{n,p} = \sqrt{D_{n,p}\tau_{n,p}} \quad (10)$$

$$D_{n,p} = \frac{K_B T}{q}\mu_{n,p} \quad (11)$$

where $L_{n,p}$ and $\mu_{n,p}$ are diffusion length and mobility of electron and hole, respectively. Additionally, D, K_B, and q are diffusivity, Boltzmann constant, and charge, respectively. The role of the thickness of $MASnI_3$ active layer on PCE, $\tau_{n,p}$ and $L_{n,p}$, is displayed in Fig. 10(a). The figure reveals that with greater thickness, the PCE improves. At the N_t of 10^{14} cm^{-3}, the $L_{n,p}$ is 2 μm. Considering the cost of the material, a thickness of 1 μm has been chosen at this defect density. From the Fig. 10(b) it can be seen that, the $MASnI_3$ absorbers defect has a profound role on $\tau_{n,p}$ and $L_{n,p}$. When N_t ranges from 10^{10} cm^{-3} to 10^{18} cm^{-3}, a significant decrease in $\tau_{n,p}$ and $L_{n,p}$ is observed. At the impurity state of 10^{10} cm^{-3}, $\tau_{n,p}$ and $L_{n,p}$ stands at 10^7 ns and 2 $\times$ 10^2 μm. However, at N_t of 10^{18} cm^{-3}, these characteristics dramatically drop to 0.1 ns and 0.02 μm. This results indicates that both the degradation of PV performance and the increase in carrier recombination losses at surfaces and interfaces are highly sensitive to even minor changes in N_t due to the rapid decay of $\tau_{n,p}$ and $L_{n,p}$.[79,94–96]

3.5. Effect of interface defect state on the performance of designed PSC

In this numerical simulation of $MASnI_3$-based PSC, the influence of defect density at the $Zn_3P_2/MASnI_3$ and $WS_2/MASnI_3$ junctions is examined. Fig. 11(a) illustrates the role of N_t at the interface of $Zn_3P_2/MASnI_3$ on the overall PV cell performance. In this analysis, the defect density is changed from 10^7 cm^{-3} to 10^{17} cm^{-3}. Both the PCE and FF remain stable at 32.31% and 87.35%, respectively, reaching to the density of 10^{10} cm^{-3}. However, beyond this point, they decrease to 27.54% for PCE and 85.36% for FF. Similarly, the values of V_{oc} and J_{sc} stay unchanged at 1.08 V and 34.20 mA cm^{-2} up to a defect density of 10^{10} cm^{-3}. Once the N_t exceeds this threshold, the values of V_{oc} and J_{sc} begin to decline, reaching 1.03 V and 31.15 mA cm^{-2}, respectively, as the N_t increases further. Therefore, the variation in defects at the $Zn_3P_2/MASnI_3$ junction has a significant impact on the performance of the PV device.[31,39,66,69,91] Furthermore, the influence of defect density at the $WS_2/MASnI_3$ interface on output metrics of designed PV devices is assessed by varying it from 10^8 to 10^{18} cm^{-3}. Fig. 11(b) demonstrates the impact of interface defect density on the photovoltaic characteristics. Clearly seen from the picture that no change in performance characteristics occurs until the defect density exceeds 10^{15} cm^{-3}. As the defect state

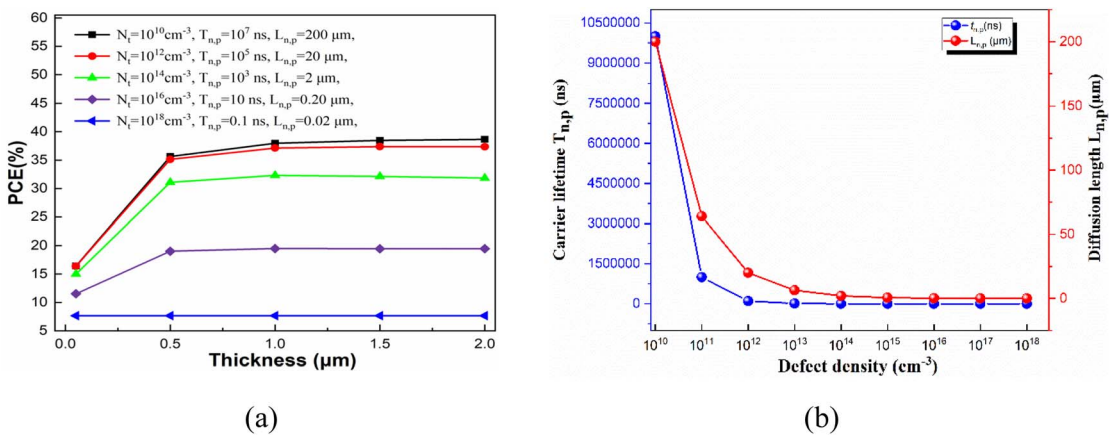

Fig. 10 Impact of absorber layer (a) thickness and (b) defect density on charge carrier's lifetime ($\tau_{n,p}$) and diffusion length ($L_{n,p}$).

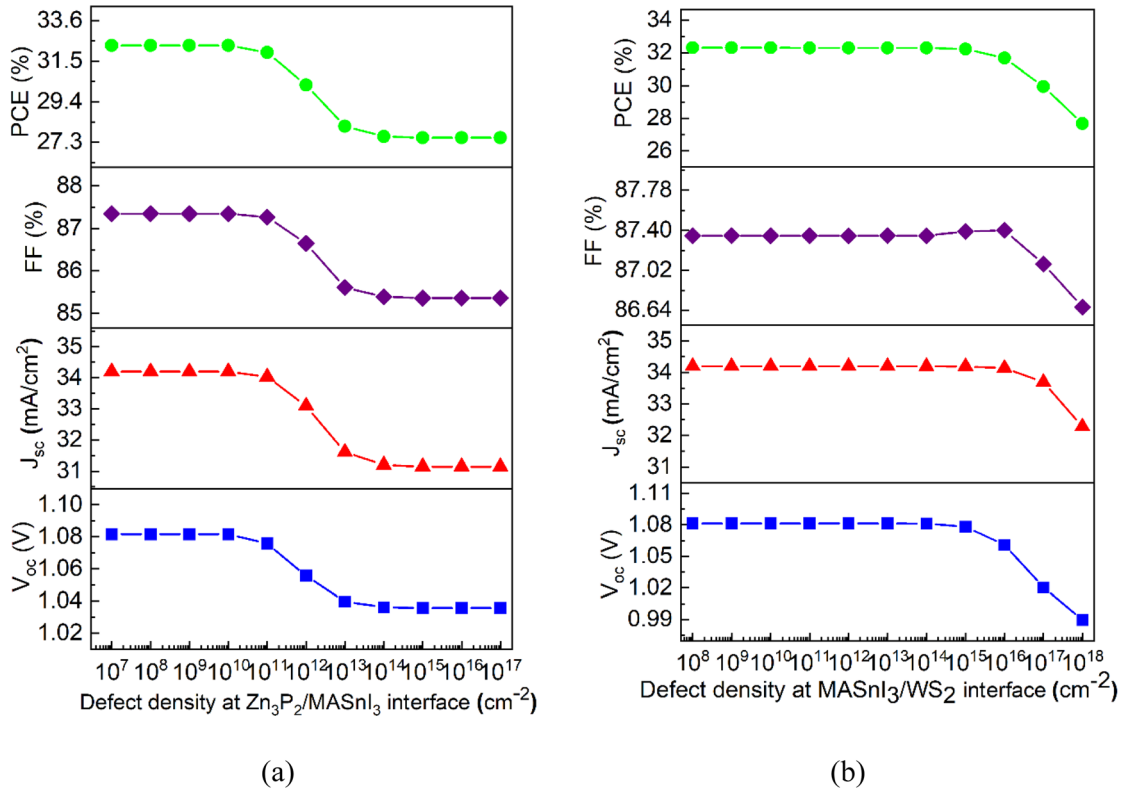

Fig. 11 Impact of defect density at the interface of (a) Zn_3P_2/MASnI$_3$ and (b) MASnI$_3$/WS_2 on cell performance.

rises from 10^{16} to 10^{18} cm^{-3}, the V_{oc} declines from 1.08 to 0.98 V. As a consequence, the PCE drops from 32.31% to 26.96%, and the J_{sc} experiences a reduction to 31.62 mA cm^{-2}. The decreased cell efficiency can be ascribed to greater carrier recombination, which is most likely attributable to the increased defect density at the junction.[39,66,69] The findings clearly demonstrate that interface defects play a critical role in determining PV device performance. To enhance the PCE of the proposed MASnI$_3$ solar device, an optimal defect density of 10^{10} cm^{-2} is applied at both the MASnI$_3$/Zn_3P_2 and WS_2/MASnI$_3$ interfaces.

3.6. *C–V* and *C–F* characteristics of the proposed PV device

To optimize the device's characteristics, it is essential to thoroughly understand the capacitance–voltage (*C–V*) and capacitance–frequency (*C–F*) characteristics of the proposed MASnI$_3$-based PSC. The *C–V* properties of a solar module provide critical insights into its electrical behavior, material properties, and junction characteristics. These include interface and surface effects, capacitive response under varying biases, depletion region width, and the built-in potential.[97] By evaluating the capacitance under different bias voltages, we can study the interaction between an AC signal and a DC-biased p–n junction, offering valuable information about the dynamic charge behavior across the junction.[98] In this study, the total capacitance and shunt resistance at the interface of structure are modeled as parallel elements in the equivalent circuit. However, describing the entire cell as a single p–n junction is not a reliable approximation, as the proposed solar module is composed of multiple thin-film layers. Therefore, to capture the influence of secondary p–n junctions within the device, *C–V* curves have been computed for both the overall architecture and the MASnI$_3$/ETL p–n junction. To investigate the effects of deep-level defects, *C–V* simulations have performed at 1 MHz, since higher frequencies inhibit the ability of these defect states to follow the rapidly oscillating AC voltage. Fig. 12(a) depicts the *C–V* characteristics of the whole device. As illustrated, the applied voltage causes the capacitance to gradually grow. Notably, when the applied voltage is more than 0.5 V, an apparent rise in capacitance is evident, whereas the increase is more gradual below this threshold. Furthermore, Fig. 12(a) (inset) presents the Mott–Schottky sketch for the studied device. According to the Mott–Schottky relation, the built-in voltage (V_{bi}) can be calculated from the correlation between surface capacitance (C) and N_A on the p-doped side of the p–n junction.[51,86] The built-in voltage (V_{bi}) is identified at the intersection point between the extrapolated linear region of the Mott–Schottky plot and the midpoint of the voltage axis.[98–101] Ideally, V_{oc} of a device should match this intrinsic voltage. However, in practice, the measured V_{oc} is typically lower, which can be attributed to internal recombination losses within the device.[52] In this study, the estimated value of V_{bi} is 1.16 V for the proposed device structure, where the V_{oc} of the device is 1.08 V.

The capacitance–frequency (*C–F*) characteristics, as depicted in Fig. 12(b), the output efficiency of the device is also crucially enhanced by their involvement. In this analysis, the evaluation of capacitance is carried out against frequency, keeping the temperature constant at 300 K, with no external bias

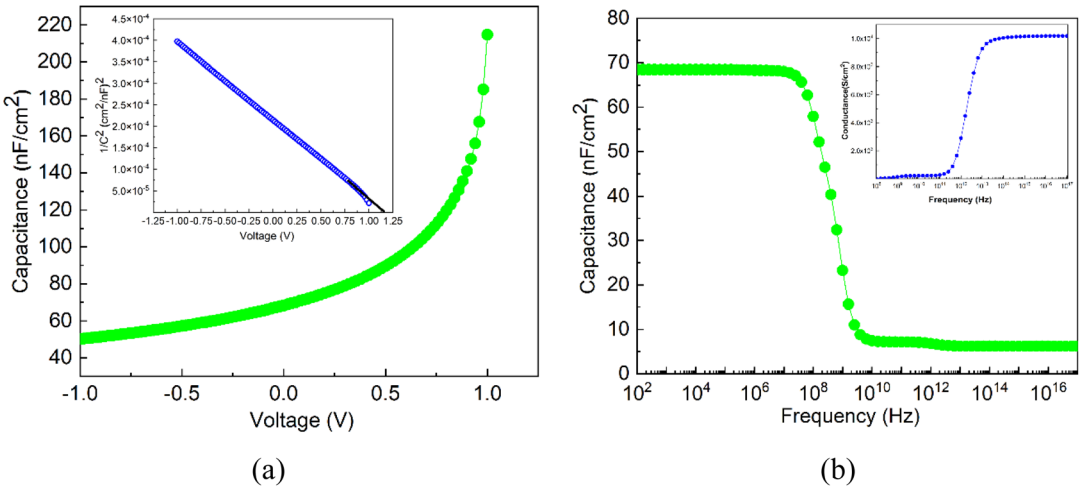

Fig. 12 (a) The C–V and (b) C–F properties of proposed $MASnI_3$-based solar cells.

applied.[98,100–102] The capacitance declines sharply with increasing frequency and eventually stabilizes at a lower level beyond approximately 10^{10} Hz, can clearly be seen in Fig. 12(b). The frequency between 10^2 to 10^8 Hz have the largest capacitance values, after which a steep decline is noted as the frequency approaches and surpasses 10^{10} Hz. The inset of Fig. 12(b) further exhibits the conductance behavior of the PSC device across different operating frequencies. The conductance–frequency plot indicates that the device demonstrates minimal conductance at lower frequencies. However, as the frequency increases, a noticeable rise in conductance begins around 10^{14} Hz, after which it reaches a plateau, indicating stabilization.

3.7. Impact of operating temperature and work function on performance of proposed PSC

The performance and long-term stability of PSCs are highly affected by variations in operating temperature, which affects both the physical properties of the perovskite absorber and the interfacial charge dynamics. In our research, we have

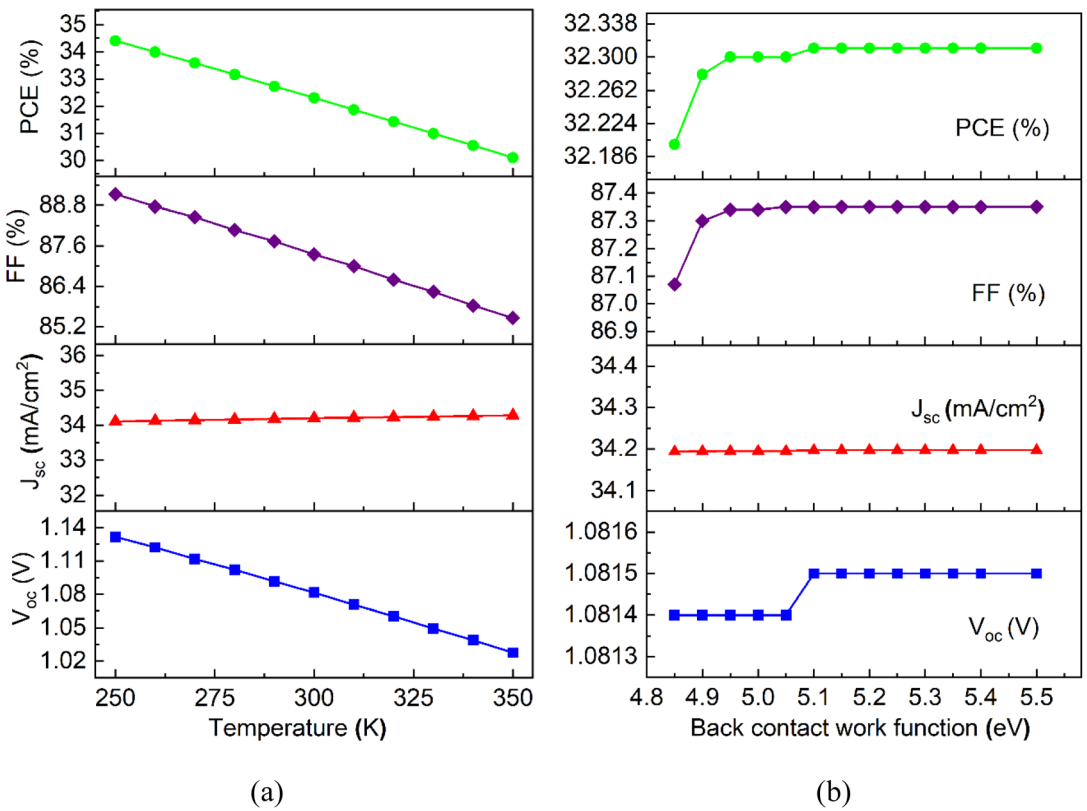

Fig. 13 Impact of (a) operating temperature and (b) work function on the properties of the designed PSC.

investigated the performance of the device under varying operating temperatures, systematically ranging from 250 K to 350 K and illustrates in Fig. 13(a). From the figure, it is apparent that, with the exception of the J_{sc}, all other photovoltaic performance parameters (PCE, FF, V_{oc}) exhibit a linear decline as the operating temperature increases. Higher temperatures result in an increased generation of photo generated charge carriers, leading to an enhancement in the J_{sc}. However, the associated narrowing of the bandgap energy shortens the mean free path of the carriers, potentially affecting charge transport and collection efficiency.[103,104] Here, the V_{oc} exhibited a decrease, shifting from 1.13 V at 250 K to 1.02 V at 350 K, reflecting the impact of temperature-induced changes in the reverse saturation current and recombination processes.[105] Between 250 K and 350 K, the operating temperature increase causes the PCE of the proposed heterojunction PSC to decline from 34.4% to 30.1%, with the FF simultaneously decreasing from 89.13% to 85.46%. On the other hand, J_{sc} slightly increases from 34.1 mA cm^{-2} to 34.27 mA cm^{-2}. Following the evaluation of temperature-dependent behavior, the simulation is conducted at an operational set point of 300 K, yielding optimized PV metrics with an efficiency of 32.30%, FF of 87.35%, J_{sc} of 34.19 mA cm^{-2} and V_{oc} of 1.08 V.

Back-contact materials with an appropriate work function (WF) are essential for efficient charge extraction, thereby directly impacting the performance of solar cells. It defines the energy barrier for carrier injection or extraction at the interfaces between the electrode and the active layers. In particular, a proper band alignment of the rear electrode WF with the energy levels of the transport layers facilitates efficient carrier collection and reduces energy losses due to reduced interfacial recombination. This work considers the role of the back contact WF with its influence clearly demonstrated in Fig. 13(b). Here, the rear electrode WF is adjusted between 4.85 and 5.55 eV to examine how it affects device performance. Fig. 13(b) illustrates that all PV performance parameters rise with the back contact WF up to 5.1 eV, after that there is no significant fluctuation. As the back-electrode work function increases, carrier barrier heights at the back interface are reduced, leading to improved charge extraction and enhanced device performance.[76] As rear contact work function increases, the creation of back ohmic contact of the heterojunction device, rather than a Schottky contact, helps in increasing solar cell output. This transition allows for more efficient hole collection from the absorber layer.[35,93] This observation suggests that employing a rear contact with a WF exceeding 5.1 eV facilitates optimal energy level alignment, therefore improving the suggested $MASnI_3$ PSCs overall performance. Consequently, Ni is selected as the back electrode, owing to its work function of 5.35 eV.[61] Ni is a compelling option for the back electrode in solar cell technology due to its favorable work function, chemical and thermal stability, and compatibility with common HTLs, all of which contribute to improved device performance and longevity.[61]

3.8. Impact of parasitic resistances on the performances of proposed device

This study also examines how the series resistance (R_s) and shunt resistance (R_{sh}) influence the performance of $MASnI_3$-based heterojunction PSCs. The corresponding J–V characteristics are presented in Fig. 14(a) and (b). Series resistance (R_s) mainly originates from the electrical interconnections among the device terminals, as well as from the resistive losses in the back metal and front contacts of the heterojunction solar cell. In contrast, the reverse saturation current generated by fabrication-related defects within the solar cell is a major factor influencing the shunt resistance (R_{sh}). The solar cell exhibits its best performance under conditions of minimized series resistance (R_s) and maximized shunt resistance (R_{sh}). Elevated R_s decreases the fill factor, and very high R_s can additionally reduce the short-circuit current.[74,91] In this study, varying R_s from 0 to 5 Ω cm^2 leads to a noticeable reduction in J_{sc}, causing the PCE to drop from 32.30% to 26.9% under a constant R_{sh} of 10^5 Ω cm^2. Hence, reducing R_s is crucial for maintaining high photovoltaic efficiency. Fig. 14(b) presents the effect of varying shunt resistance (R_{sh}) on the electrical outputs of the device. Solar power loss occurs when the photogenerated current is diverted through alternative pathways created by low shunt resistance. Such deviation leads to a decline in both the junction voltage and the current generated within the solar cell.

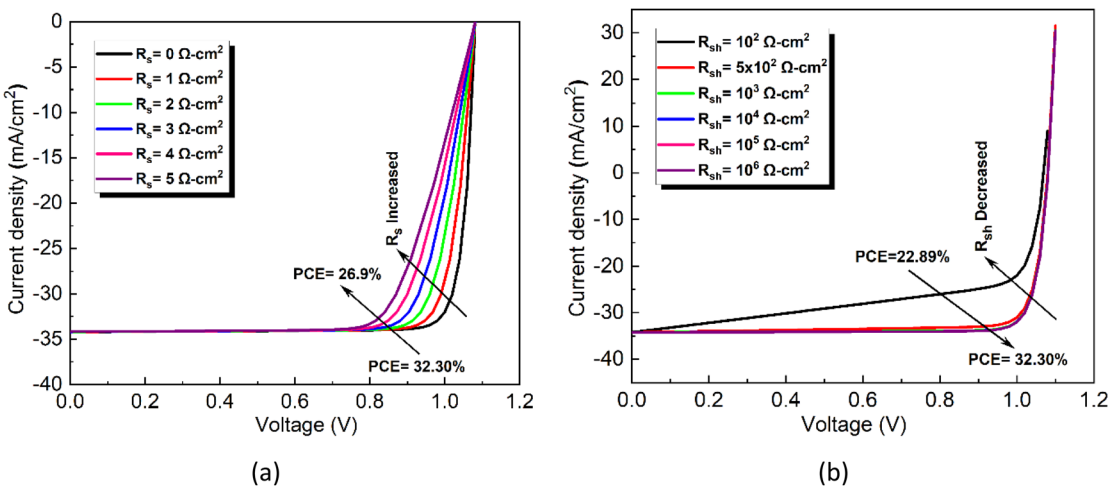

Fig. 14 Effect of (a) series and (b) shunt resistance on $MASnI_3$-based heterojunction PSCs.

Therefore, preserving a high R_{sh} value is critical to reducing power losses and enhancing the overall performance of the device. Here, R_{sh} is raised from 100 to 10^6 Ω cm^2 while R_s remains constant at 0.5 Ω cm^2. With R_{sh} set at 100 Ω cm^2 and 10^6 Ω cm^2, the proposed solar cell exhibits PCEs of 22.89% and 32.30%, respectively. It is evident from the figure that increasing shunt resistance improves both the PCE and the *J*–*V* response.

3.9. Cell characteristics through various ML algorithm

In this section, a comparison is conducted among three ML models to evaluate their effectiveness in predicting the efficiency of photovoltaic devices. To gain deeper insights into each model's behavior—particularly with respect to overfitting or underfitting—parity plots were employed to visualize predictions on both training and testing datasets. These plots illustrate the

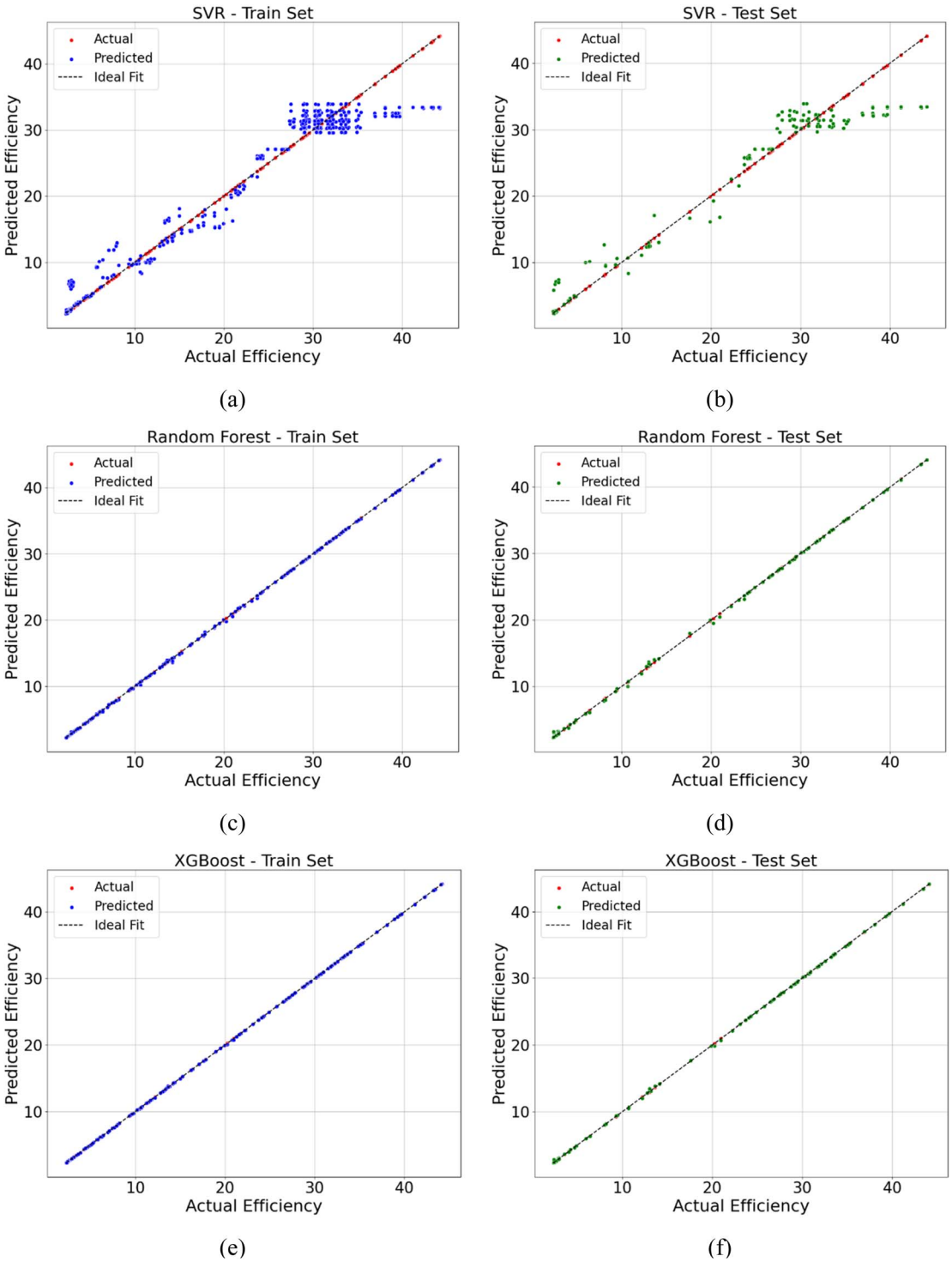

Fig. 15 Parity plot for training and testing data of various algorithms.

Table 5 A summary of the accuracy of the ML models

Performance metric	SVR		RF		XGBoost	
	Training	Testing	Training	Testing	Training	Testing
MSE	14.56	12.94	0.068	0.032	0.0103	0.0092
MAE	3.17	2.63	0.41	0.18	0.078	0.051
R^2	0.8902	0.9145	0.9991	0.9998	0.9995	0.9999

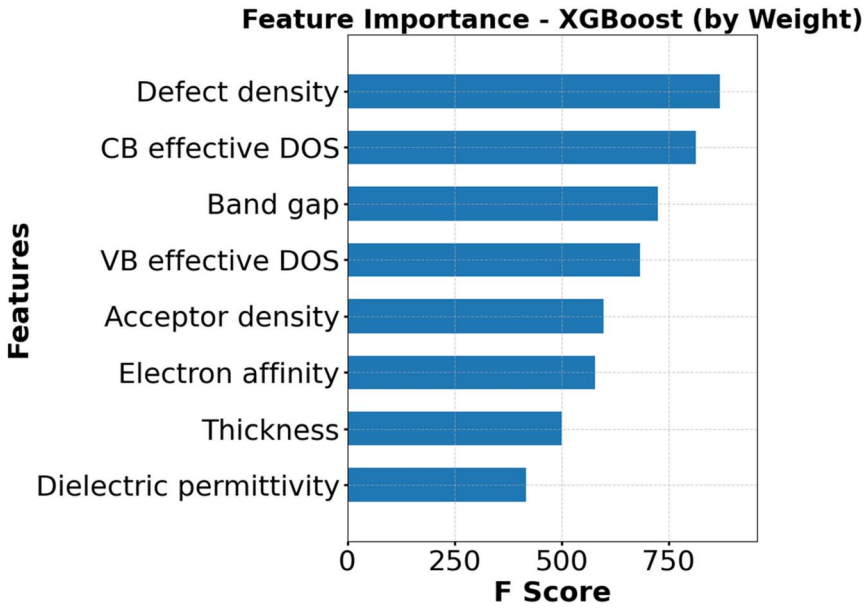

Fig. 16 Feature importance using XGBoost algorithm based on the weight metric.

relationship between actual and predicted efficiency values, with a diagonal reference line indicating the ideal fit, thereby enabling an intuitive visual assessment of model performance. Fig. 15 presents the parity plots for training and testing data across the three regression-based ML models. In addition, Table 5 summarizes the performance metrics, including the coefficient of determination (R^2), mean squared error (MSE), and mean absolute error (MAE). Based on both the visual and quantitative evaluations suggesting that XGBoost attains the highest predictive accuracy, yielding an R^2 value of 0.9999, along with a low MSE of 0.0092 and MAE of 0.051 on the testing dataset.

In order to assess the impacts of material properties on the PCE of the proposed PSC, it is essential to evaluate the relative importance of the features.[43,106] In this study, feature importance was calculated using the XGBoost algorithm based on the weight metric, as illustrated in Fig. 16. Feature importance by weight in XGBoost refers to the number of times a feature is used to split the data across all the trees in the model. It is one of the simplest and most intuitive ways to measure feature importance. The more frequently a feature is used to create a split, the higher its importance score by weight. This method provides a quick overview of which features the model relies on most often during the training process. As shown in the figure, among the eight considered features, defect density exhibits the highest importance score by weight, indicating that it plays the most significant role in influencing the model's prediction of photovoltaic device efficiency.

Table 6 Various physical parameters optimized for the proposed $MASnI_3$-based PSC

Optimized parameters (unit)	WS_2 ETL	$MASnI_3$ absorber	Zn_3P_2 HTL	Junction defect density	
				$MASnI_3/WS_2$	$Zn_3P_2/MASnI_3$
Thickness (μm)	0.05	1.0	0.1		
N_D (cm^{-3})	10^{18}	—	—		
N_A (cm^{-3})	—	10^{17}	10^{18}		
N_t (cm^{-3})	10^{15}	10^{14}	10^{15}		
$\sigma_{n,p}$ (cm^2)				10^{-19}	10^{-19}
Total density (cm^{-2})				10^{10}	10^{10}

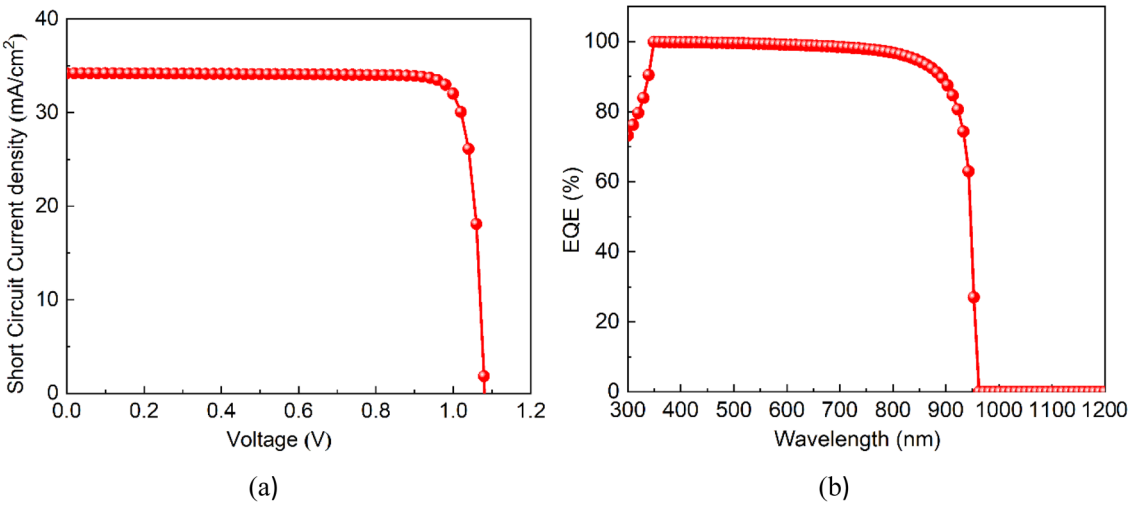

Fig. 17 Optimized (a) *J–V* characteristics and (b) EQE spectral response of $MASnI_3$-based PSC.

Table 7 PV performance parameters of $MASnI_3$-based PSCs: comparison of earlier studies and the current investigation

Configurations	Research area	V_{oc} (V)	J_{sc} (mA cm^{-2})	FF (%)	PEC (%)	Ref.
FTO/TiO_2/$MASnI_3$/Spiro-OMeTAD/Au	Exp.	0.88	16.8	0.42	6.4	21
FTO/TiO_2/$MASnI_{3-x}Br_x$/Spiro-OMeTAD/Au	Exp.	0.68	16.30	0.48	5.23	22
FTO/TiO_2/$MASnI_{3-x}P_xI_3$/Spiro-OMeTAD/Au	Exp.	0.72	15.18	50.07	5.44	23
FTO/compact TiO_2/mp-TiO_2/$MASnI_3$/PTAA/Au	Exp.	0.49	22.91	0.64	7.13	24
FTO/TiO_2/$MASnI_3$/Cu_2O/Au	Theo.	1.20	25.97	87.79	27.43	29
ITO/ZnO/$CH_3NH_3SnI_3$/Spiro-OMeTAD/Au	Theo.	1.81	14.29	75.95	19.66	107
Au/$CH_3NH_3SnI_3$/CIGS/TiO_2/ZnO:Al	Theo.	0.86	41.84	80.02	28.69	30
Al/FTO/WS_2/$MASnI_3$/Zn_3P_2/Ni	Theo.	1.08	32.30	87.35	32.30	This work

3.10. Overall PV performance of the proposed $MASnI_3$-based PSC

A detailed numerical investigation is presented in this research for a novel architecture of perovskite solar cells comprising Al/FTO/WS_2/$MASnI_3$/Zn_3P_2/Ni heterojunction structure. Here, Zn_3P_2 is introduced as an HTL to significantly reduce rear-side recombination and improve carrier collection. The various physical parameters optimized in this research are illustrated in Table 6. With an absorber thickness of 1 μm for $MASnI_3$ and 0.1 μm for the Zn_3P_2 HTL, along with their respective doping concentrations of 10^{17} cm^{-3} and 10^{18} cm^{-3} we achieve an enhanced performance in the $MASnI_3$-based PSC. Fig. 17(a) shows the *J–V* characteristics of the proposed Al/FTO/WS_2/$MASnI_3$/Zn_3P_2/Ni heterojunction. Furthermore, the device performance is reflected in the EQE response, as shown in Fig. 17(b). The $MASnI_3$ cells incorporating WS_2 as the ETL demonstrate improved EQE primarily due to favorable band alignment and reduced interfacial recombination rather than increased optical transparency.[72] Although WS_2 has a band gap of approximately 2.1 eV and absorbs part of the visible spectrum, its superior electronic properties facilitate efficient charge transfer. In addition, the Zn_3P_2 HTL enhances the EQE in the 700–900 nm region due to the back-surface field formed at the Zn_3P_2/$MASnI_3$ interface, which improves carrier collection. As expected, the EQE drops to zero beyond 950 nm, where the photon energy falls below the band gap of the absorber. Additionally, Table 7 represents the comparison of different experimental and theoretical $MASnI_3$-based device structures. Among them, our proposed structure demonstrates a remarkable PCE of 32.30%, with FF of 87.35%, V_{oc} of 1.08 V, and J_{sc} of 34.19 mAcm^{-2}. This theoretical analysis provides an overall guideline for the researcher of perovskite solar cell technology to develop environmentally friendly highly efficient, and cost-effective $MASnI_3$-based PV devices.

4. Conclusion

In this numerical study, a novel lead-free $MASnI_3$-based perovskite solar cell is designed, and its photovoltaic performance is investigated using the SCAPS-1D simulation tool. Initially, several ETLs and HTLs are introduced and their band alignment and performance metrics are evaluated. Among them, WS_2 as ETL and Zn_3P_2 as HTL have emerged as optimal candidates because of their favorable band alignments, low toxicity, and efficient charge transport properties; consequently, recombination losses are minimized at both the front and rear interfaces, resulting in an impressive PV performance. Additionally, carrier lifetime and diffusion length characteristics regarding the $MASnI_3$ absorber layer thickness and defect density are examined here. Moreover, the impact of temperature, metal work function, and defect density of the perovskite/

ETL and HTL/perovskite interfaces on the PV output characteristics is investigated to improve the device performance. After optimizing all the device parameters, an outstanding efficiency of 32.30%, an FF of 87.35%, a V_{oc} of 1.08 V, and a J_{sc} of 34.19 mA cm^{-2} are obtained with an absorber thickness of 1.0 μm, an acceptor density of 10^{17} cm^{-3}, and a defect density of 10^{14} cm^{-3}. Finally, three machine learning methods are employed to predict the efficiency of the designed PV device as well as to determine the relative importance of individual physical parameters. Among the three algorithms, XGBoost outperforms the remaining two algorithms (SVR and RF) with an impressive R^2 value of 0.9999 and a lower MSE of 0.0092. However, from the analysis it is seen that defect density exerts the greatest influence on device performance, and the predicted efficiencies closely match the simulation outcomes. These results highlight the promise of integrating theoretical modeling with AI-driven optimization to advance the design of stable, efficient, and eco-friendly lead-free perovskite solar cells.

Conflicts of interest

There are no conflicts to declare.

Data availability

The dataset generated and analysed during this study is available at: https://github.com/TM-Khan-9/MASnI3-perovskite-solar-cell/blob/MASnI3-perovskite-solar-cell/ML.xlsx, while the Notebook containing the full modelling and analysis code is available at: https://github.com/TM-Khan-9/MASnI3-perovskite-solar-cell/blob/MASnI3-perovskite-solar-cell/IMPLEMENTATION.ipynb. All materials are openly accessible through the GitHub repository.

Acknowledgements

The authors are grateful to Dr Marc Burgelman from the University of Gent in Belgium for providing the SCAPS-1D modeling program.

References

1 A. K. Sharma and D. K. Kaushik, Numerical simulation of $MASnI_3$/CuI heterojunction based perovskite solar cell, *J. Phys.:Conf. Ser.*, 2022, **2267**, 012001.
2 G. Cao, X. Gu, J. Su, Z. He and B. Tang, Boosting the efficiency of lead-free $MASnI_3$ perovskite solar cells through a bilayer CIGS structure approximating a gradient bandgap distribution, *J. Mater. Chem. A*, 2025, **13**, 10187–10196.
3 A. K. Jena, A. Kulkarni and T. Miyasaka, Halide perovskite photovoltaics: background, status, and future prospects, *Chem. Rev.*, 2019, **119**, 3036–3103.
4 P. Panda, S. Beriha and S. K. Tripathy, Design of $MASnI_3$ perovskite solar cell with chalcogenide ETLs to achieve high photo conversion efficiency of 31.51% using SETFOS, *Optik*, 2024, **296**, 170093.
5 J. P. Correa-Baena, M. Saliba, T. Buonassisi, M. Grätzel, A. Abate, W. Tress and A. Hagfeldt, Promises and challenges of perovskite solar cells, *Science*, 2017, **358**, 739–744.
6 P. Saha, S. Singh and S. Bhattacharya, Performance optimization of $MASnI_3$ perovskite solar cells: insights into device architecture, *Micro Nanostruct.*, 2024, **191**, 207827.
7 A. Kojima, K. Teshima, Y. Shirai and T. Miyasaka, Organometal halide perovskites as visible-light sensitizers for photovoltaic cells, *J. Am. Chem. Soc.*, 2009, **131**, 6050–6051.
8 M. A. Green, E. D. Dunlop, M. Yoshita, N. Kopidakis, K. Bothe, G. Siefer, D. H. M. Rauer, J. Hohl-Ebinger and X. Hao, Solar cell efficiency tables (Version 64), *Prog. Photovoltaics Res. Appl.*, 2024, **32**, 425–441.
9 S. B. Ivriq, M. H. Mohammadi and R. S. Davidsen, Enhancing photovoltaic efficiency in half-tandem $MAPbI_3$/$MASnI_3$ perovskite solar cells with triple core–shell plasmonic nanoparticles, *Sci. Rep.*, 2025, **15**, 1478.
10 F. Arif, M. Aamir, A. Shuja, M. Shahiduzzaman and J. Akhtar, Simulation and numerical modeling of high-performance $CH_3NH_3SnI_3$ solar cell with cadmium sulfide ETL by SCAPS-1D, *Result Opt.*, 2024, **14**, 100595.
11 M. Lazemi, S. Asgharizadeh and S. Bellucci, A computational approach to interface engineering of lead-free $CH_3NH_3SnI_3$ highly efficient perovskite solar cells, *Phys. Chem. Chem. Phys.*, 2018, **20**, 25683–25692.
12 T. M. Koh, T. Krishnamoorthy, N. Yantara, C. Shi, W. L. Leong, P. P. Boix, A. C. Grimsdale, A. G. Mhaisalkar and N. Mathewa, Formamidinium tin-based perovskite with low Eg for photovoltaic applications, *J. Mater. Chem. A*, 2015, **3**, 14996–15000.
13 K. P. Marshall, R. I. Walton and R. A. Hatton, Tin perovskite/fullerene planar layer photovoltaics: improving the efficiency and stability of lead-free devices, *J. Mater. Chem. A*, 2015, **3**, 11631–11640.
14 K. Sekar, R. Manisekaran, O. M. Nwakanma and M. Babudurai, Significance of formamidinium incorporation in perovskite composition and its impact on solar cell efficiency: a mini-review, *Adv. Energy Sustain. Res.*, 2024, **5**, 2400003.
15 C. J. Bartel, C. Sutton, B. R. Goldsmith, R. Ouyang, C. B. Musgrave, L. M. Ghiringhelli and M. Scheffler, New tolerance factor to predict the stability of perovskite oxides and halides, *Sci. Adv.*, 2019, **5**, eaav0693.
16 M. H. Miah, M. U. Khandaker, M. B. Rahman, M. Nur-E-Alam and M. A. Islam, Band gap tuning of perovskite solar cells for enhancing efficiency and stability: issues and prospects, *RSC Adv.*, 2024, **14**, 15876–15906.
17 D. Ji, S. Z. Feng, L. Wang, S. Wang, M. Na, H. Zhang, C. Zhang and X. Li, Regulatory tolerance and octahedral factors using vacancy in $APbI_3$ perovskites, *Vacuum*, 2019, **164**, 186–193.
18 M. Nishat, M. K. Hossain, M. R. Hossain, S. Khanom, F. Ahmed and M. A. Hossain, Role of metal and anions in organometal halide perovskites $CH_3NH_3MX_3$ on structural

and optoelectronic properties, *RSC Adv.*, 2022, **12**, 13281–13294.

19 Q. Wang, A. Hiratsuka and S. Iikubo, Electronic properties and defect investigation of $MASnX_3$ (X = Cl, Br, I) perovskites, *ACS Appl. Energy Mater.*, 2025, **8**, 9788–9795.

20 S. A. A. Shah, M. H. Sayyad, K. Khan, K. Guo, F. Shen, J. Sun, A. K. Tareen, Y. Gong and Z. Guo, Progress towards high-efficiency and stable tin-based perovskite solar cells, *Energies*, 2020, **13**, 5092.

21 N. K. Noel, S. D. Stranks, A. Abate, C. Wehrenfennig, S. Guarnera, A. A. Haghighirad, A. Sadhanala, G. E. Eperon, S. K. Pathak, M. B. Hohnston, A. Petrozza, L. M. Herz and H. J. Sanith, Lead-free organic–inorganic tin halide perovskites for photovoltaic applications, *Energy Environ. Sci.*, 2014, **7**, 3061–3068.

22 F. Hao, C. C. Stoumpos, D. H. Cao, R. P. H. Chang and M. G. Kanatzidis, Lead-free solid-state organic–inorganic halide perovskite solar cells, *Nat. Photonics*, 2014, **8**, 489–494.

23 F. Hao, C. C. Stoumpos, R. P. H. Chang and M. G. Kanatzidis, Anomalous bandgap behavior in mixed Sn–Pb perovskites enables broadening of absorption spectrum, *J. Am. Chem. Soc.*, 2014, **136**, 8094–8099.

24 F. Li, C. Zhang, J. H. Huang, H. Fan, H. Wang, P. Wang, C. Zhan, C. M. Liu, X. Li, L. M. Yang, Y. Song and K. J. Jiang, A cation-exchange approach for the fabrication of efficient methylammonium tin iodide perovskite solar cells, *Angew. Chem., Int. Ed.*, 2019, **58**, 6688–6692.

25 K. D. Jayan and V. Sebastian, Comprehensive device modelling and performance analysis of MASnI3 based perovskite solar cells with diverse ETM, HTM and back metal contacts, *Sol. Energy*, 2021, **217**, 40–48.

26 S. A. A. Jafri, R. S. Almufarij, A. Ashfaq, R. Saleh Alqurashi, L. G. Alharbe and A. R. Abd-Elwahed, Enhancing photovoltaic efficiency: Integrating graphene and advanced interface layers to reduce the recombination losses in lead-free $MASnI_3$ perovskite solar cells, *Sol. Energy*, 2024, **270**, 112391.

27 H. Mouhib, A. Ait Hssi, Y. Ait Wahmane, L. Atourki, A. Elfanaoui and A. Ihlal, Numerical investigation of eco-friendly $MASnI_3$-based solar cell: effect of defect density and HTL, *Model. Simulat. Mater. Sci. Eng.*, 2022, **30**, 035011.

28 M. F. Hossain, M. M. Rahman, M. Harun-Or-Rashid, M. Amami, L. Ben Farhat and M. F. Rahman, Probing the impact of four BSF layers on $MASnI_3$ lead-free perovskite solar cells for >33% efficiency, *Adv. Theory Simul.*, 2024, **8**, 2400662.

29 A. K. Singh, S. Srivastava, A. Mahapatra, J. K. Baral and B. Pradhan, Performance optimization of lead-free $MASnI_3$ based solar cell with 27% efficiency, *Opt. Mater.*, 2021, **117**, 111193.

30 I. Mohanty, S. Mangal and U. P. Singh, Performance optimization of lead-free $MASnI_3$/CIGS heterojunction solar cell with 28.7% efficiency, *Opt. Mater.*, 2021, **122**, 111812.

31 T. M. Khan, B. Islam, M. M. Rahaman, M. Md Shakil, M. F. Rahman and S. R. Al Ahmed, Predictive design and performance analysis of lead-free $CH_3NH_3SnI_3$-based perovskite solar cells through a combination of SCAPS-1D and machine learning based modelling, *Sol. Energy Mater. Sol. Cells*, 2025, **282**, 113388.

32 M. K. Omrani, M. Minbashi, N. Memarian and D. H. Kim, Improving CZTSSe solar cell performance using a SnS BSF layer, *Solid State Electron.*, 2018, **141**, 50–57.

33 S. Khosroabadi and S. H. Keshmiri, Design of high-efficiency ultrathin CdS/CdTe solar cell using BSF and Bragg reflector, *Opt. Express*, 2014, **22**, A921–A931.

34 B. Maharana, R. Jha and S. Chatterjee, Metal oxides as buffer layers for CZTS solar cells: a numerical SCAPS-1D analysis, *Opt. Mater.*, 2022, **131**, 112734.

35 S. R. Al Ahmed, M. Rahaman, A. Sunny, S. Rahman, M. S. Islam, T. T. Abd El-Mohaymen, Z. A. Alrowaili and M. S. Mian, Enhancing the efficiency of Cu_2Te thin-film solar cell with WS_2 buffer layer: a simulation study, *Opt. Laser Technol.*, 2023, **159**, 108942.

36 S. R. Al Ahmed, Investigation on the performance enhancement of heterojunction SnS thin-film solar cell with a Zn_3P_2 hole transport layer and a TiO_2 electron transport layer, *Energy Fuels*, 2024, **38**, 1462–1476.

37 T. N. Fridolin, D. K. G. Maurel, G. W. Ejuh, T. T. Bénédicte and N. J. Marie, Optimizing CIGSe solar cell performance: Cu(In,Ga)Se_2–ZnS case study, *J. King Saud Univ. Sci.*, 2019, **31**, 1404–1413.

38 W. Li, W. Li, Y. Feng and C. Yang, Numerical analysis of the back interface for high efficiency wide band gap chalcopyrite solar cells, *Sol. Energy*, 2019, **180**, 207–215.

39 Y. Cao, X. Zhu, H. Chen, X. Zhang, J. Zhou, Z. Hu and J. Pang, Towards high-efficiency inverted Sb_2Se_3 thin-film solar cells, *Sol. Energy Mater. Sol. Cells*, 2019, **200**, 109942.

40 A. Sunny and S. R. Al Ahmed, Numerical simulation and performance evaluation of highly efficient Sb_2Se_3 solar cell with SnS HTL, *Phys. Status Solidi B*, 2021, **258**, 2100400.

41 A. Ahmed, K. Riaz, H. Mehmood, T. Tauqeer and Z. Ahmad, Performance optimization of $CH_3NH_3Pb(I_{1-x}Br_x)_3$-based perovskite solar cells by comparing different ETL materials through conduction band offset engineering, *Opt. Mater.*, 2020, **105**, 109897.

42 M. Marzia Khatun, M. N. Hossain Riyad, S. Rahman, A. Sunny, A. Hosen, and S. R. Al Ahmed, *Numerical Simulation of Highly-Efficient Lead-free Tin-Based Perovskite Solar Cell with Sb_2S_3 as Novel Hole Transport Layer*, IEECP'21, Silicon Valley, San Francisco, CA-USA, 2021.

43 M. S. Islam, M. T. Islam, S. Sarker, H. Al Jame, S. S. Nishat, M. R. Jani, A. Rauf, S. Ahsan, K. M. Shorowordi, H. Efstathiadis, J. Carbonara and S. Ahmed, Machine learning approach to delineate the impact of material properties on solar cell device physics, *ACS Omega*, 2022, **7**, 22263–22278.

44 D. Sadhu, D. Dattatreya, A. Deo, K. Tarafder and D. De, Performance prediction and analysis of perovskite solar cells using machine learning, *J. Alloy Compd. Commun.*, 2024, **3**, 100022.

45 H. Al Jame, S. Sarker, M. S. Islam, M. T. Islam, A. Rauf, S. Ahsan, S. S. Nishat, M. R. Jani, K. M. Shorowordi,

J. Carbonara and S. Ahmed, Supervised machine learning-aided SCAPS-based quantitative analysis for optimum bromine doping in methylammonium tin-based perovskite ($MASnI_{3-x}Br_x$), *ACS Appl. Mater. Interfaces*, 2022, **14**, 502–516.

46 T. M. Khan, A. Hosen, O. Saidani and S. R. Al Ahmed, Artificial neural network assisted numerical analysis on performance enhancement of $Sb_2(S,Se)_3$ solar cell with SnS as HTL, *Mater. Today Commun.*, 2024, **40**, 109639.

47 F. Li, X. Peng, Z. Wang, Y. Zhou, Y. Wu, M. Jiang and P. M. Xu, Machine learning-assisted design and fabrication for solar cells, *Energy Environ. Mater.*, 2019, **2**, 280–291.

48 I. I. Malek, H. Imtiaz and S. Subrina, Machine learning driven performance enhancement of perovskite solar cells with CNT as both hole transport layer and back contact, *Sol. Energy*, 2024, **278**, 112737.

49 N. Shrivastav, A. Abu-Jrai, P. Kanjariya, H. Hassan, A. Verma, J. Madan and R. Pandey, Advanced computational techniques for optimizing manganese-based perovskite solar cells: From SCAPS-1D simulations to machine learning predictions, *J. Electron. Mater.*, 2024, **54**, 7.

50 A. Ghosh, M. Moumita, M. A. Bappy, N. L. Dey, M. Aktarujjaman, M. M. Islam Jim, N. S. Awwad and H. A. Ibrahium, Machine learning-driven SCAPS modeling for optimizing $CH_3NH_3SnBr_3$ perovskite solar cells, *Langmuir*, 2025, **41**, 11215–11237.

51 T. M. Khan and S. R. Al Ahmed, Investigating the performance of $FASnI_3$-based perovskite solar cells with various electron and hole transport layers: Machine learning approach and SCAPS-1D analysis, *Adv. Theory Simul.*, 2024, **7**, 2400353.

52 P. S. B. Sadanand, P. K. Singh, A. K. Thakur and D. K. Dwivedi, Optimization of photovoltaic solar cell performance via earth-abundant Zn_3P_3 back surface field, *Optik*, 2021, **229**, 166235.

53 K. Sobayel, M. Shahinuzzaman, N. Amin, M. R. Karim, M. A. Dar, R. Gul, M. Alghoul, K. B. Sopian, A. K. M. Hasan and M. Akhtaruzzaman, Efficiency enhancement of CIGS solar cell by WS_2 as window layer through numerical modelling, *Sol. Energy*, 2020, **207**, 479–485.

54 M. K. S. Bin Rafiq, N. Amin, H. F. Alharbi, M. Luqman, A. Ayob, Y. S. Alharthi, N. H. Alharthi, B. Bais and M. Akhtaruzzaman, WS_2: a new window layer material for solar cell application, *Sci. Rep.*, 2020, **10**, 771.

55 M. Burgelman, K. Decock, A. Niemegeers, J. Verschraegen and S. Degrave, *SCAPS Manual*, Univ. Gent, 2019, pp. 1–111.

56 T. Alzoubi and M. Moustafa, Simulation analysis of functional $MoSe_2$ layer for ultra-thin $Cu(In,Ga)Se_2$ solar cells, *Mod. Phys. Lett. B*, 2020, **34**, 2050065.

57 S. Karthick, S. Velumani and J. Bouclé, Experimental and SCAPS simulated formamidinium perovskite solar cells: A comparison of device performance, *Sol. Energy*, 2020, **205**, 349–357.

58 T. Minemoto, Y. Kawano, T. Nishimura and J. Chantana, Numerical reproduction of a perovskite solar cell by device simulation considering band gap grading, *Opt. Mater.*, 2019, **92**, 60–66.

59 F. Ayala-Mató, O. Vigil-Galán, M. M. Nicolás-Marín and M. Courel, Study of loss mechanisms on $Sb_2(S_{1-x}\ Se_x)_3$ solar cells with n-i-p structure: Toward an efficiency promotion, *Appl. Phys. Lett.*, 2021, **118**, 073903.

60 M. S. Salem, A. Shaker, T. S. Almurayziq and M. T. Alshammari, Prospective efficiency boosting of full-inorganic single-junction $Sb_2(S,Se)_3$ solar cell, *Sol. Energy Mater. Sol. Cells*, 2022, **248**, 112001.

61 H. B. Michaelson, The work function of the elements and its periodicity, *J. Appl. Phys.*, 1977, **48**, 4729–4733.

62 N. S. Khalid, S. R. How, J. Lias and M. K. Ahmad, Effect of deposition temperature on fluorine-doped tin oxide thin films by spray pyrolysis, *Appl. Mech. Mater.*, 2015, **773–774**, 652–656.

63 M. Jafari, M. M. Shahidi and M. H. Ehsani, Effect of substrate temperature on properties of WS_2 thin films, *Sci. Rep.*, 2025, **15**, 21561.

64 Y. Yu, D. Zhao, C. R. Grice, W. Meng, C. Wang, W. Liao, A. J. Cimaroli, H. Zhang, K. Zhu and Y. Yan, Thermally evaporated methylammonium tin triiodide thin films for lead-free perovskite solar cell fabrication, *RSC Adv.*, 2016, **6**, 90248–90254.

65 K. Kakishita, T. Baba and T. Suda, Zn_3P_3 thin films grown on glass substrates by MOCVD, *Thin Solid Films*, 1998, **334**, 25–29.

66 S. R. Al Ahmed, A. Sunny and S. Rahman, Performance enhancement of Sb_2Se_3 solar cells using a back surface field layer, *Sol. Energy Mater. Sol. Cells*, 2021, **221**, 110919.

67 B. Ezealigo, A. C. Nwanya, A. Simo, R. U. Osuji, R. Bucher, M. Maaza and F. Ezema, Optical and electrochemical properties of CuI thin film deposited by SILAR, *Arab. J. Chem.*, 2019, **12**, 5380–5391.

68 X. Liu, K. Yan, D. Tan, X. Liang, H. Zhang and W. Huang, Solvent engineering improves efficiency of tin-based perovskite solar cells, *ACS Energy Lett.*, 2018, **3**, 2701–2707.

69 M. M. Khatun, A. Sunny and S. R. Al Ahmed, Numerical investigation on performance improvement of WS_2 thin-film solar cell with copper iodide as hole transport layer, *Sol. Energy*, 2021, **224**, 956–965.

70 P. Jackson, R. Wuerz, D. Hariskos, E. Lotter, W. Witte and M. Powalla, Effects of heavy alkali elements in Cu(In,Ga) Se_2 solar cells with efficiencies up to 22.6%, *Phys. Status Solidi RRL*, 2016, **10**, 583–586.

71 T. M. Khan, M. A. Shams, M. M. Khatun, J. H. Chowdhury, M. S. Uddin, T. A. Emon, M. M. Shakil and S. R. A. Ahmed, Predictive modeling and optimization of WS_2 thin-film solar cells: A comprehensive study integrating machine learning, deep learning and SCAPS-1D approaches, *Renewable Energy*, 2025, **252**, 123519.

72 A. Hosen, S. Yeasmin, K. M. S. Bin Rahmotullah, M. F. Rahman and S. R. Al Ahmed, Design and simulation of a highly efficient $CuBi_2O_4$ thin-film solar

cell with hole transport layer, *Opt. Laser Technol.*, 2024, **169**, 110073.

73 M. Gloeckler and J. R. Sites, Efficiency limitations for wide-bandgap chalcopyrite solar cells, *Thin Solid Films*, 2005, **480–481**, 241–245.

74 B. Islam, A. Hosen, T. M. Khan, M. F. Rahman, M. H. Rahman and M. S. Islam, Simulating the effect of inserting Sb_2S_3 as hole transport layer on sns-based thin-film solar cells, *J. Electron. Mater.*, 2024, **53**, 4726–4739.

75 S. Rabhi, G. M. Alsulaim, Y. I. Bouderbala and M. W. Alam, Enhancing inverted perovskite solar cells: The role of o-OMe-PEAI interlayer in performance with MXene as alternative front contacts, *Inorg. Chem. Commun.*, 2025, **175**, 114096.

76 M. Atowar Rahman, Enhancing the photovoltaic performance of Cd-free Cu_2ZnSnS_4 heterojunction solar cells using SnS HTL and TiO_2 ETL, *Sol. Energy*, 2021, **215**, 64–76.

77 S. Rabhi, T. Hidouri, S. Goumri-Said, H. J. Alathlawi, G. M. Alsulaim and M. W. Alam, Bifacial perovskite solar cells with> 21% efficiency: Computational insights into novel HTLs materials and architectures, *Sol. Energy*, 2024, **284**, 113083.

78 S. Rabhi, A. BaQais, S. Sadaf and M. W. Alam, Unlocking high efficiency and superior bifacial performance in semi-transparent inverted perovskite solar cells: harnessing MXene and innovative materials for next-generation energy devices, *Surf. Interfaces*, 2025, **73**, 107439.

79 T. M. Khan, B. Islam and S. R. Al Ahmed, Performance analysis and optimization of SnSe thin-film solar cell with Cu_2O HTL through a combination of SCAPS-1D and machine learning approaches, *Mater. Today Commun.*, 2024, **41**, 110490.

80 A. Guerrero, J. Bisquert and G. Garcia-Belmonte, Impedance spectroscopy of metal halide perovskite solar cells, *Chem. Rev.*, 2021, **121**, 14430–14484.

81 K. Sekar, L. Marasamy, S. Mayarambakam, H. Hawashin, M. Nour and J. Bouclé, Lead-free, formamidinium germanium-antimony halide ($FA_4GeSbCl_{12}$) double perovskite solar cells: the effects of band offsets, *RSC Adv.*, 2023, **13**, 25483–25496.

82 M. Bag, L. A. Renna, R. Y. Adhikari, S. Karak, F. Liu, P. M. Lahti, T. P. Russell, M. T. Tuominen and D. Venkataraman, Kinetics of ion transport in perovskite active layers and its implications for active layer stability, *J. Am. Chem. Soc.*, 2015, **137**, 13130–13137.

83 F. Galatopoulos, A. Savva, I. T. Papadas and S. A. Choulis SA, The effect of hole transporting layer in charge accumulation properties of p-i-n perovskite solar cells, *APL Mater.*, 2017, **5**, 076102.

84 L. Peng and W. Xie, Theoretical and experimental investigations on the bulk photovoltaic effect in lead-free perovskites $MASnI_3$ and $FASnI_3$, *RSC Adv.*, 2020, **10**, 14679–14688.

85 F. Opoku, K. K. Govender, C. G. C. E. Van Sittert and P. P. Govender, Role of MoS_2 and WS_2 monolayers on photocatalytic hydrogen production and the pollutant degradation of monoclinic $BiVO_4$: a first-principles study, *New J. Chem.*, 2017, **41**, 11701–11713.

86 E. Z. Stutz, S. P. Ramanandan, M. Flór, R. Paul, M. Zamani and E. S. Steinvall, Stoichiometry modulates the optoelectronic functionality of zinc phosphide ($Zn_{3-x}P_{2+x}$), *Faraday Discuss.*, 2022, **239**, 202–218.

87 S. Miyake, S. Hoshino and T. Takenaka, On the phase transition in cuprous iodide, *J. Phys. Soc. Jpn.*, 2013, **7**, 19–24.

88 A. Lenz, H. Kariis, A. Pohl, P. Persson and L. Ojamäe, The electronic structure and reflectivity of PEDOT:PSS from density functional theory, *Chem. Phys.*, 2011, **3854**, 44–51.

89 M. Turcu and U. Rau, Fermi level pinning at CdS/$Cu(In,Ga)(Se,S)_2$ interfaces: effect of chalcopyrite alloy composition, *J. Phys. Chem. Solids*, 2003, **64**, 1591–1595.

90 A. Hosen, M. S. Mian and S. R. A. Ahmed, Simulating the performance of a highly efficient $CuBi_2O_4$-based thin-film solar cell, *SN Appl. Sci.*, 2021, **3**, 5.

91 M. R. Sultana, B. Islam and S. R. A. Ahmed, Modeling and performance analysis of highly efficient copper indium gallium selenide solar cell with Cu_2O hole transport layer using SCAPS-1D, *Phys. Status Solidi A*, 2022, **219**, 5.

92 B. Zhou, X. Yin, J. Zhang, G. Zeng, B. Li and J. Zhang, Numerical simulation of an innovative high-efficiency solar cell with CdTe/Si composite absorption layer, *Opt. Mater.*, 2020, **110**, 110505.

93 A. Hosen and S. R. A. Ahmed, Performance analysis of SnS solar cell with a hole transport layer based on experimentally extracted device parameters, *J. Alloys Compd.*, 2022, **909**, 164823.

94 H. I. Alkhammash, M. Mottakin, M. M. Hossen, M. Akhtaruzzaman and M. J. Rashid, Design and defect study of $Cs_2AgBiBr_6$ double perovskite solar cell using suitable charge transport layers, *Semicond. Sci. Technol.*, 2022, **38**, 015005.

95 S. Cao, Y. He, M. M. Islam, S. Chen, A. Islam and T. Sakurai, Numerical investigation of structural optimization and defect suppression for high-performance perovskite solar cells via SCAPS-1D, *Jpn. J. Appl. Phys.*, 2023, **62**, SK1052.

96 K. Sekar K, L. Marasamy, S. Mayarambakam, P. Selvarajan and J. Bouclé, Highly efficient lead-free silver bismuth iodide (Ag_3BiI_6) rudorffite solar cells with novel device architecture: a numerical study, *Mater. Today Commun.*, 2024, **38**, 108347.

97 J. Han, X. Pu, H. Zhou, Q. Cao, S. Wang and Z. He, Synergistic effect through the introduction of inorganic zinc halides at the interface of TiO_2 and Sb_2S_3 for high-performance Sb_2S_3 planar thin-film solar cells, *ACS Appl. Mater. Interfaces*, 2020, **12**, 44297–44306.

98 A. Srivastava, S. K. Tripathy, T. R. Lenka and V. Goyal, Numerical simulations of novel quaternary chalcogenide $Ag_2MgSn(S/Se)_4$-based thin-film solar cells using SCAPS-1D, *Sol. Energy*, 2022, **239**, 337–349.

99 J. C. Nolasco, A. Sánchez-Díaz, R. Cabŕ, J. Ferŕ-Borrull, L. F. Marsal and E. Palomares, Relation between the barrier interface and the built-in potential in pentacene/C_{60} solar cell, *Appl. Phys. Lett.*, 2010, **97**, 013305.

100 Sadanand, P. K. Singh, S. Rai, P. Lohia and D. K. Dwivedi, Comparative study of the CZTS, $CuSbS_2$ and $CuSbSe_2$ solar photovoltaic cells with an earth-abundant non-toxic buffer layer, *Sol. Energy*, 2021, **222**, 175–185.

101 A. Srivastava, S. K. Tripathy, T. R. Lenka, P. Hvizdos, P. S. Menon, F. Lin and A. G. Aberle, Device simulation of Ag_2SrSnS_4 and $Ag_2SrSnSe_4$ based thin-film solar cells from scratch, *Adv. Theory Simul.*, 2022, **5**, 2100208.

102 S. R. Meher, L. Balakrishnan and Z. C. Alex, Analysis of Cu_2ZnSnS_4/CdS based photovoltaic cell: a numerical simulation approach, *Superlattices Microstruct.*, 2016, **100**, 703–722.

103 P. Singh and N. M. Ravindra, Temperature dependence of solar cell performance – an analysis, *Sol. Energy Mater. Sol. Cells*, 2012, **101**, 36–45.

104 Y. P. Varshni, Temperature dependence of the energy gap in semiconductors, *Physica*, 1967, **34**, 149–154.

105 H. Zhou, Q. Chen, G. Li, S. Luo, T. B. Song, H. S. Duan, Z. Hong, J. You, Y. Liu and Y. Yang, Interface engineering of highly efficient perovskite solar cells, *Science*, 2014, **345**, 542–546.

106 R. Kundara and S. Baghel, Predictive design of $KSnI_3$-based perovskite solar cells using SCAPS and machine learning model, *Mater. Sci. Eng., B*, 2024, **307**, 117536.

107 N. Bala and S. K. Mallik, Comparative study of lead-free perovskite materials $MASnI_3$, $MASnBr_3$ and $MAGeI_3$ to design, simulate and optimize lead-free PSC, *Indian J. Pure Appl. Phys.*, 2024, **62**, 292–303.